The Santa Lúcia Cu-Au deposit, Carajás Mineral Province, Brazil: a Neoarchean (2.68 Ga) member of the granite-related copper-gold systems of Carajás

Mineralium Deposita

The Santa Lúcia Cu-Au Deposit, Carajás Province, Brazil: A Neoarchean (2.68 Ga) Member of the Granite-related Copper-Gold Systems of Carajás

--Manuscript Draft--

Manuscript Number:	MIDE-D-19-00209R4
Full Title:	The Santa Lúcia Cu-Au Deposit, Carajás Province, Brazil: A Neoarchean (2.68 Ga) Member of the Granite-related Copper-Gold Systems of Carajás
Article Type:	Regular Articles
Corresponding Author:	Raphael Bianchi Hunger, M.D. State University of Campinas Campinas, São Paulo BRAZIL
Corresponding Author Secondary Information:	
Corresponding Author's Institution:	State University of Campinas
Corresponding Author's Secondary Institution:	
First Author:	Raphael Bianchi Hunger, M.D.
First Author Secondary Information:	
Order of Authors:	Raphael Bianchi Hunger, M.D.
	Gustavo Henrique Coelho de Melo
	Roberto Perez Xavier
	Carolina Penteado Natividade Moreto
	Cristina Talavera
	Zhi-Kun Su
	Xin-Fu Zhao
Order of Authors Secondary Information:	
Funding Information:	
Abstract:	The Santa Lúcia copper-gold deposit lies in the southeastern portion of the Carajás Mineral Province, along NW-SE splays of the Carajás Fault. The deposit is hosted by a rhyolitic subvolcanic rock, which is crosscut by pegmatite intrusions. The paragenetic evolution at Santa Lúcia encompasses an early stage of chlorite alteration, followed by potassic alteration with microcline, greisenization (quartz-muscovite-tourmaline), copper-gold ore precipitation and late sericite and hematite vein formation/fracture infill. Copper mineralization is dominantly represented by chalcopyrite-sphalerite-pyrrhotite-pentlandite-pyrite breccias, which are spatially associated with greisen alteration and characterized by the enrichment of light rare earth elements (LREE), Ni, Co, and Cr. The alteration types, mineralization styles and ore assemblage suggest that the Santa Lúcia deposit could represent a member of the Paleoproterozoic (ca. 1.88 Ga) granite-related copper-gold systems of Carajás (e.g., the Breves and Estrela deposits). However, the in-situ U-Pb analyses of ore-related monazite yield a weighted average 207 Pb/ 206 Pb age of 2688 ± 27 Ma, thereby constraining the timing of mineralization at Santa Lúcia to the Neoarchean. Moreover, tourmaline from the pegmatite and within the ore zones have a range of δ 11 B values from -3.7 to -0.6‰, therefore linked to a magmatic boron source. Collectively, these results indicate that the Santa Lúcia deposit is the first reduced magmatic-hydrothermal, iron oxide-poor system formed in the Neoarchean, coeval with the 2.72–2.68 Ga metallogenic event responsible for the genesis of important iron oxide copper-gold (IOCG) deposits in the Carajás Mineral Province.
Response to Reviewers:	Dear Editor,

	The Figure Captions were placed in the right section, as requested. Sincerely, Raphael Hunger

The Santa Lúcia Cu-Au Deposit, Carajás Mineral Province, Brazil: A Neoarchean (2.68 Ga) Member of the Granite-related Copper-Gold Systems of Carajás

Raphael B. Hunger [1], Gustavo H. C. de Melo [2], Roberto P. Xavier [1], Carolina P. N. Moreto [1], Cristina Talavera [3], Zhi-Kun Su [4], Xin-Fu Zhao [4]

[1] Institute of Geosciences, University of Campinas, 250 Carlos Gomes, Campinas, São Paulo 13083-855, Brazil

[2] Department of Geology - Morro do Cruzeiro Campus, Federal University of Ouro Preto, Nove Street, Ouro Preto 35400-000, Brazil

[3] Grant Institute - King's Buildings, The University of Edinburgh, James Hutton Road, Edinburgh EH9 3FE, United Kingdom

[4] State Key Laboratory of Geological Processes and Mineral Resources, and Faculty of Earth Resources, China University of Geosciences, 388 Lumo Road, Wuhan 430074, China

Abstract

The Santa Lúcia copper-gold deposit lies in the southeastern portion of the Carajás Mineral Province, along NW-SE splays of the Carajás Fault. The deposit is hosted by a rhyolitic subvolcanic rock, which is crosscut by pegmatite intrusions. The paragenetic evolution at Santa Lúcia encompasses an early stage of chlorite alteration, followed by potassic alteration with microcline, greisenization (quartz-muscovite-tourmaline), copper-gold ore precipitation and late sericite and hematite vein formation/fracture infill. Copper mineralization is dominantly represented by chalcopyrite-sphalerite-pyrrhotite-pentlandite-pyrite breccias, which are spatially associated with greisen alteration and characterized by the enrichment of light rare earth elements (LREE), Ni, Co, and Cr. The alteration types, mineralization styles and ore assemblage suggest that the Santa Lúcia deposit could represent a member of the Paleoproterozoic (ca. 1.88 Ga) granite-related copper-gold systems of Carajás (e.g., the Breves and Estrela deposits). However, the *in-situ* U-Pb analyses of ore-related monazite yield a weighted average $^{207}Pb/^{206}Pb$ age of 2688 ± 27 Ma, thereby constraining the timing of mineralization at Santa Lúcia to the Neoarchean. Moreover, tourmaline from the pegmatite and within the ore zones have a range of $\delta^{11}B$ values from -3.7 to -0.6‰, therefore linked to a magmatic boron source. Collectively, these results indicate that the Santa Lúcia deposit is the first reduced magmatic-hydrothermal, iron oxide-poor system formed in the Neoarchean, coeval with the 2.72–2.68 Ga metallogenic event responsible for the genesis of important iron oxide copper-gold (IOCG) deposits in the Carajás Mineral Province.

Keywords Santa Lúcia • Granite-related Cu-Au deposits • Carajás Domain • U-Pb geochronology • Boron isotopes

Corresponding author: raphael.hunger@gmail.com; phone: +55 19 996674875; ORCID ID: 0000-0003-3712-8406

Introduction

The Carajás Mineral Province (CMP), in the Amazonian Craton, is among the best-endowed metal provinces in the world. It hosts an extensive number of copper-gold deposits that may be separated into world-class (100 Mt – 1,1 Bt) iron oxide copper-gold systems (or IOCG; e.g., Salobo, Igarapé Bahia/Alemão, Cristalino, Sossego-Sequeirinho) and granite-related Cu-Au-(W-Bi-Sn) systems (e.g., Breves, Águas Claras, and Estrela), generally of smaller tonnage (< 50 Mt) (Xavier et al. 2012; Pollard et al. 2019). Geochronological data indicate that the IOCG deposits formed in multiple episodes during the Neoarchean (2.72–2.68 Ga and 2.57 Ga) and Paleoproterozoic (1.90–1.87 Ga). Conversely, the Cu-Au-(W-Bi-Sn) deposits are typically shallow hydrothermal systems whose origin has been particularly linked to the widespread Paleoproterozoic (ca. 1.88 Ga) A-type granite magmatism event registered in the province (Grainger et al. 2008; Moreto et al. 2015a, b).

There is enough evidence that the Paleoproterozoic copper-gold deposits, regardless of their class, were formed synchronously with the voluminous ca. 1.88 Ga A-type granites recognized in the Amazonian Craton (e.g., Central Carajás, Breves, Pojuca, and Young Salobo; Wirth et al. 1986; Machado et al. 1991; Tallarico et al. 2004). Similarly, the ca. 2.5 Ga IOCG deposits (e.g., Salobo, Igarapé Bahia/Alemão, Grota Funda; Tallarico et al. 2005; Melo et al. 2016, 2019; Hunger et al. 2018) seem to be temporally coincident with the emplacement of ca. 2.5 Ga A-type granites in the northern sector of the CMP (e.g., Old Salobo, Itacaiúnas, and GT-46 granites; Machado et al. 1991; Souza et al. 1996; Toledo et al. 2019). Conversely, the mineralization event at 2.72–2.68 Ga, recorded in several IOCG deposits of the Southern Copper Belt (e.g. Sequeirinho-Pista, Bacuri, and Bacaba; Moreto et al. 2015a, b), does not overlap with the widespread ca. 2.76–2.73 Ga anorogenic granitic intrusions identified in the province, such as the Plaquê, Planalto, and Serra do Rabo suites (Sardinha et al. 2006; Feio et al. 2012, 2013).

Collectively, these data point to a temporal coincidence between the formation of copper-gold deposits and events of granite magmatism (i.e., ca. 2.5 Ga and 1.88 Ga) in the CMP, with an exception for the early Neoarchean (ca. 2.70 Ga). The genetic link between hydrothermal fluids of magmatic origin and copper mineralization, which seems to be more straightforward for the Paleoproterozoic systems, has not yet been clarified for deposits formed at this particular metallogenic epoch (Xavier et al. 2017). Consequently, the genesis of magmatic-hydrothermal copper systems in the early Neoarchean still needs to be better substantiated.

The Santa Lúcia deposit (5–14 Mt at 1.4–2.0% Cu, 0.2–0.4 g/t Au; OZ Minerals 2019) lies within the Southern Copper Belt, along with several 2.7 Ga IOCG deposits and in a region dominated by 2.76–2.73 Ga granite intrusions (e.g., Plaquê and Planalto suites; **Figs. 1 and 2**). The deposit shares a number of similarities with the granite-related copper-gold deposits of Carajás (e.g., Breves and Estrela), including the association with shear zones, intense greisen-like alteration, and iron oxide-poor ore assemblage. However, the geological context of the Santa Lúcia deposit,

together with its anomalous Ni-Co-Cr-enriched ore signature, may suggest a distinct metallogenetic evolution from those copper-gold deposits typically linked with granite-related systems.

This study aims to characterize the Santa Lúcia host rocks, the spatial distribution and types of hydrothermal alteration, the ore paragenesis, and its geochemical and boron isotope signatures. Furthermore, this study places constraints on the age of the mineralization via SHRIMP II U-Pb geochronology. These data contribute new insights into the timing of formation of the granite-related deposits in the CMP, revealing the existence of an older (Neoarchean) mineralizing event also responsible for the genesis of this type of copper-gold systems in the province.

Geological Setting of the CMP

The CMP constitutes one of the best preserved cratonic nuclei in the world (**Fig. 1A**). Formed and tectonically stabilized during the Neoarchean (Teixeira et al. 1989; Tassinari 1996; Tassinari and Macambira 1999, 2004), it comprises two Archean domains: Rio Maria, in the south, and Carajás, in the north (**Fig. 1B**); separated by a regional and geophysically constrained E-W tectonic discontinuity (Feio et al. 2013).

In the Carajás Domain (**Fig. 1C**), Mesoarchean (2974 ± 15 Ma; Avelar et al. 1999) orthogneisses and migmatites from the Xingu Complex, and the Chicrim-Cateté Orthogranulite (Ricci and Carvalho 2006; Vasquez et al. 2008) encompass the oldest basement rocks. Additionally, a series of Mesoarchean (ca. 3.0–2.83 Ga) granitoids, including the Bacaba and Campina Verde tonalites, the Rio Verde trondhjemite, and the Canaã dos Carajás, Cruzadão, Bom Jesus and Serra Dourada granites (Moreto et al. 2011; Feio et al. 2013; Rodrigues et al. 2014), are also considered as part of the basement.

Neoarchean (ca. 2.76–2.74 Ga) volcano-sedimentary sequences attributed to the Itacaiúnas Supergroup (Wirth et al. 1986; DOCEGEO 1988; Machado et al. 1991) and the Rio Novo Group (Hirata et al. 1982) overlie the basement rocks of the Carajás Domain. The Itacaiúnas Supergroup is divided into four units, designated as Igarapé Salobo, Grão Pará, Igarapé Bahia, and Igarapé Pojuca groups (DOCEGEO 1988). According to Tavares et al. (2018), these sequences can be simply divided, from bottom to top, into volcanic rocks, banded iron formation, and clastic-sedimentary association.

Apparently above an angular unconformity, the Águas Claras Formation overlaps the Itacaiúnas Supergroup and represents its Archean unmetamorphosed, siliciclastic cover. It mainly consists of sandstones, siltstones, and orthoconglomerates deposited in fluvial to shallow marine environments (Nogueira et al. 1995).

Mafic-ultramafic magmatism in the Carajás Domain is represented by the Luanga layered complex (2763 ± 6 Ma; Machado et al. 1991) and the Cateté Intrusive Suite. The latter is subdivided into the Serra da Onça, Serra do Puma, Serra do Jacaré-Jacarezinho, Vermelho and Igarapé Carapanã bodies (Macambira and Vale 1997; Macambira and Ferreira Filho 2002; Ferreira Filho et al. 2007).

Three main episodes of granitic intrusion have been identified in the Carajás Domain, represented by intrusive bodies that cut both supracrustal sequences and the Mesoarchean basement rocks: (i) ca. 2.76–2.73 Ga syntectonic, foliated, A-type subalkaline and calc-alkaline granite, comprising the Plaquê, Planalto, Estrela, Serra do Rabo, Igarapé-Gelado and Pedra Branca suites (Avelar et al. 1999; Huhn et al. 1999; Barros et al. 2004, 2009; Sardinha et al. 2006; Feio et al. 2012, 2013); (ii) ca. 2.57 Ga peralkaline to metaluminous granite, represented by the Old Salobo, Itacaiúnas and the GT-46 granites (Machado et al. 1991; Souza et al. 1996; Toledo et al. 2019); and; (iii) ca. 1.88 Ga A-type alkaline to subalkaline and metaluminous to slightly peraluminous granite of the Serra dos Carajás Intrusive Suite (Central de Carajás, Young Salobo, Cigano, Pojuca, Breves, and Rio Branco granites; Machado et al. 1991; Tallarico et al. 2004).

At least three tectonic models have been proposed to describe the evolution of the Carajás Domain: (i) formation of a pull-apart basin (Carajás Basin) during a dextral transtension, subsequently tectonically inverted to positive flower structures by sinistral transpression (Araújo et al. 1988); (ii) formation during continental rifting related to mantle-plume activity (Tallarico 2003); and; (iii) formation in a volcanic arc setting related to subduction processes (Meirelles 1986; Dardenne et al. 1988; Meirelles and Dardenne 1991; Teixeira 1994; Lobato et al. 2005; Silva et al. 2005; Teixeira et al. 2010). According to Tavares et al. (2018), the recurrence of collisional-extensional events taking place from the Neoarchean (2.76–2.52 Ga) to the Paleoproterozoic (2.09–1.88 Ga) allowed the establishment of a rift-related system and subsequent formation of volcano-sedimentary sequences in the Carajás Domain, which evolved upon a previously stabilized basement substrate (ca. 2.87 to 2.83 Ga).

Overview of the Granite-related Cu-Au Deposits of Carajás

The Carajás Domain contains the largest concentration of high-tonnage copper-gold deposits of the world (Monteiro et al. 2008; Xavier et al. 2012). The most economically important deposit-type in this domain is represented by the world-class IOCG systems, that together with smaller targets and prospects comprise an estimated reserve of more than 8 Gt of copper-gold ore (Xavier et al. 2017). Secondarily, there is a smaller group of deposits, all medium- to small-sized (< 50 Mt), typically characterized by a polymetallic Cu-Au-(W-Bi-Sn) association. Representative members of this class include the Breves (50 Mt @ 1.22 wt.% Cu, 0.75 g/t Au; Tallarico et al. 2004), Águas Claras (9.5 Mt @ 2.43 g/t Au; Soares et al. 1994; Silva and Villas 1998) and Estrela (30 Mt @ 0.5 wt.% Cu; DOCEGEO 2002) deposits, interpreted to be genetically associated with A-type Paleoproterozoic (ca. 1.88 Ga) granitic intrusions. Major differences from the IOCG deposits encompass: (i) lack or small concentration of iron-oxides (e.g., magnetite); (ii) low fS_2 ore paragenesis (e.g., pyrite ± pyrrhotite); (iii) discrete or absence of sodic-calcic alteration; (iv) pervasive quartz and muscovite alteration zones; and; (v) geochemical signature suggesting more elevated values of granitophile elements such as W, Sn, Bi, Be and Li (Tallarico et al. 2004; Grainger et al. 2008; Xavier et al. 2017; Pollard et al.

2019). Previous genetic models proposed for these deposits include greisen-type systems associated with granitic cupolas (Tallarico et al. 2004), intrusion-related systems (Xavier et al. 2005) and hybrid systems evolved from the interaction of reduced magmatic and meteoric fluids with oxidized country rocks (e.g., alkaline A-type granites; Botelho et al. 2005).

Comprehensive reviews of deposits from this class were conducted by Grainger et al. (2008) and more recently by Pollard et al. (2019). According to the latter, the Gameleira, Alvo 118 and Sossego-Curral deposits could also be included into this group of granite-related copper-gold systems, although being currently considered shallower and/or magmatic end-members of the IOCG clan (Lindenmayer et al. 2001; Chiaradia et al. 2006; Monteiro et al. 2008; Torresi et al. 2012).

Sampling and Analytical Methods

Field work, Petrography, and SEM

The study of the Santa Lúcia deposit (6º29'S 49º42'W) involved the systematic description of samples from six drill holes (PPCSLUC – FD034; FD014; FD022; FD026; FD028; FD030), to determine the nature of the deposit host rocks, distribution and types of hydrothermal alteration, and modes of occurrence of the copper-gold ore. Detailed petrographic analyses were performed in twenty polished thin sections and accessory mineral phases were identified by Scanning Electron Microscope (SEM) coupled with EDS (Energy-Dispersive X-Ray Spectrometer). These studies were respectively executed at the laboratories of Microscopy and Scanning Electron Microscope of the Institute of Geosciences, University of Campinas (UNICAMP), Brazil.

Ore geochemistry

High-precision trace and REE analyses, using inductively coupled plasma-mass spectrometry (ICP-MS), were carried out in five whole rock samples representative of the main ore zone of the Santa Lúcia deposit. After being crushed and ground, 100 mg of each sample was placed into individual cylindrical refractories containing a solution of 1 ml of HNO_3 and 6 ml of HCl and subsequently submitted to a procedure of assisted reaction on a Multiwave PRO (Anton Paar) microwave system, for total dissolution. The microwave power was initially adjusted to 850 W for a period of thirty minutes. Subsequently, 0.5 ml of HF was added to the solutions and the samples returned to the microwave, readjusted to 1500 W, for thirty additional minutes. Finally, 1 ml of H_2O was added, and the previous procedure was repeated. All dissolutions were conducted using ultra-pure water (18,2 MΩ.cm), obtained from a Milli-Q system. After total dissolution, elimination of concentrated acids was performed through evaporation. The analyses were carried out in an ICP–MS XseriesII (Thermo), coupled with a CCT (Collision Cell Technology), at the Isotope Geology Laboratory of the Institute of Geosciences, UNICAMP. The detection limit (DL) was determined as the

average (x) plus 3 standard deviation (s) from ten blank samples (DL = x + 3s). Calibration of the instrument was performed using multi-elementar solutions, gravimetrically prepared via 100 mg/L mono-elementary standard-solutions (AccuStandards). Quality control was assured using the GS-N (granite – ANRT, France) standard reference material.

SHRIMP II U-Pb analyses

The *in-situ* U-Pb SHRIMP II monazite isotopic analyses were performed using the SHRIMP II at the John de Laeter Centre, Curtin University of Technology, Australia. A full description of the analytical procedure for the Curtin SHRIMP II is reported in Fletcher et al. (2010). One carbon-coated polished thin section (sample FD022/80.10) was imaged by an automated scanning electron microscope, and monazite crystals were identified using Backscattered Electron (BSE) imaging on a TESCAN TIMA instrument and Energy-dispersive spectrometry (EDS) X-ray spectra. The best monazite grains were then drilled out and mounted in epoxy discs, cleaned and gold-coated for imaging by BSE on a Mira3 FESEM instrument. A 10–15 µm diameter spot was used, with a mass-filtered O_2^- -primary beam of ~ 0.6–0.7 nA. Data for each spot were collected in sets of 8 scans on the monazites through the mass range of $^{196}LaPO_2^+$, $^{203}CePO_2^+$, $^{204}Pb^+$, Background, $NdPO_2^+$, $^{206}Pb^+$, $^{207}Pb^+$, $^{208}Pb^+$, $^{232}Th^+$, $^{245}YCeO^+$, $^{254}UO^+$, $^{264}ThO_2^+$ and $^{270}UO_2^+$. The $^{206}Pb/^{238}U$ age and U-content standards are "French" (514 Ma and 1000 ppm U and 6.3% Th; Fletcher et al. 2010) and the $^{207}Pb/^{206}Pb$ standard used to monitor instrument induced mass fractionation corresponded to the Z2908 (1796 ± 2 Ma; Fletcher et al. 2010). A fractionated correction was applied to the standard monazite (French) and unknowns, due to a slight discrepancy between the $^{207}Pb/^{206}Pb$ ratios obtained on Z2908 monazites during the SHRIMP sessions and the $^{207}Pb/^{206}Pb$ TIMS ratios. Common Pb correction was based on the measured ^{204}Pb-correction. Data were processed using the software package Isoplot 3.0 (Ludwig 2003).

Electron probe microanalyses

Electron probe microanalyses (EPMA) of tourmaline were performed on a wavelength-dispersive JEOLJXA-8100 instrument at the Center for Material Research and Analysis, Wuhan University of Technology, China. Operating conditions comprised a probe current of 20 nA, an accelerating potential of 15 kV and a beam diameter of 5 µm. Synthetic reference materials were used for calibration and include: almandine (Si and Al), rutile (Ti), rhodonite (Mn), hematite (Fe), olivine (Mg), vanadium (V), chromite (Cr), albite (Na), apatite (Ca), sanidine (K), tuhualite (Cl) and fluorite (F). Data were reduced on-line using a conventional ZAF routine. The structural formulae of tourmaline were calculated using the WinTcac software (Yavuz et al. 2014). Normalization was made on the basis of 15 cations in the tetrahedral and octahedral sites (T + Z + Y), following the suggestion of Henry and Dutrow (1996), and considering (OH + F + Cl = 4).

Boron isotope determination

Boron isotope analyses were carried out in the State Key Laboratory of Geological and Mineral Resources (GPMR), China University of Geosciences (CUG), China. Two double-polished thin sections containing tourmaline samples were investigated by optical microscopy and SEM backscattered electron imaging, aiming to select spots for laser ablation shots. Boron isotopic compositions of six tourmaline crystals were measured in situ using a Neptune Plus Laser Ablation Multi-Collector Inductively Coupled Plasma Mass Spectrometry (LA-MC-ICP-MS) and a matching New Wave UP193 laser ablation system. Detailed analytical procedures and data reduction followed those of Yang et al. (2015). Operating conditions consist of an energy density of 12 J/cm², 8 Hz repetition rates and spot diameters of 50 µm. Data were collected statistically and simultaneously in 100 cycles. Mass bias of the instrument and the fractionation of isotopes were calibrated using the standard-sample-bracketing method (SSB). The tourmaline IAEA B4 (Tonarini et al. 2003) was used as an external standard. Instrumental mass fractionation (IMF) and analytical quality were determined by replicate analyses of international tourmaline reference material IMR RB1 (Hou et al. 2010) and an in-house standard Dai ($\delta^{11}B$ = -13.6‰). The internal precision for individual analyses was typically 0.3–0.4‰ (1rsd), and external repeatability on reference samples was around 0.8‰ (1sd). The reported $\delta^{11}B$ results were calculated relative to tourmaline IAE B4 of $\delta^{11}B$ = -8.71‰ (Tonarini et al. 2003).

Geology, Hydrothermal Alteration Stages, and Mineralization

The Santa Lúcia deposit is located at the southeastern portion of the Carajás Domain, approximately 20 km northeast of the Canaã dos Carajás city, near the Serra do Rabo region. This region has a complex structural setting that represents the eastern termination of the Carajás Fault, which configures a regional WNW-ESE-trending structure that branches towards the south in NW-SE splays (Pinheiro 1997; Lima and Pinheiro 1999; Pinheiro and Holdsworth 2000; Lima 2002). In this context, the Santa Lúcia deposit lies in a valley between two S45E- and S45W-oriented plateaus, both formed by banded iron formations of the Carajás Formation (**Fig. 2**). Lithotypes characterized in the deposit area comprise a felsic subvolcanic rock, host of the mineralization and correlated to the Grão Pará Group, and intrusive pegmatite bodies (**Fig. 3**).

The subvolcanic rock represents the main lithotype of the Santa Lúcia deposit, given its wide spatial distribution. This unit is extensively affected by hydrothermal alteration and is commonly weakly to moderately mylonitized (**Fig. 4A-B**), with deformation progressively intensified in zones proximal to the pegmatite and the ore. The subvolcanic rock is greenish-to-greyish in color, and in the least deformed portions displays an aphanitic groundmass composed of quartz, potassium feldspar, biotite and subordinate oligoclase (**Fig. 5A**), that locally involves bipyramidal phenocrysts of bluish quartz (**Figs. 4C and 5B**). Bulk mineralogy indicates a rhyolitic composition. Minor amounts of zircon, monazite, and apatite are also recognized within this rock.

The pegmatite of the Santa Lúcia deposit is an intrusive body that cuts the subvolcanic rock, always defining sharp contacts generally concordant with the foliation (**Fig. 4D**), but locally oblique (**Fig. 4E**). The pegmatite is mostly pinkish-to-reddish in color, medium-to-coarse grained and displays a porphyritic texture evidenced by megacrysts of muscovite and tourmaline (**Fig. 4F-G**), both up to 6 cm in length. The mineralogy comprises quartz, potassium feldspar, plagioclase, muscovite, tourmaline (**Fig. 5C-D**) and minor amounts of molybdenite and allanite (**Fig. 5E**). Tourmaline crystals are generally poikiloblastic, riddled with fine-grained inclusions of quartz, potassium feldspar and zircon aggregates (**Fig. 5F**). Tourmaline-rich domains (up to 70 vol% tourmaline) are located within the pegmatite intrusions (**Fig. 5G**). Microcline crystals are commonly grid-twinned and in places exhibit perthitic exsolution lamellae (**Fig. 5H**). Although relatively unfoliated, deformation microstructures are commonly recognized within the pegmatite, such as quartz-subgrain formation, bent twins in feldspars and muscovite stretching and bending (**Fig. 5I**). Indications of brittle deformation include crystal fractures, micro-faults and boudinaged tourmaline crystals (**Fig. 4H**).

Hydrothermal Alteration Stages and Copper-Gold Ore

Early Chlorite-(Epidote) Alteration

Chlorite (I) crystallization is the first stage of hydrothermal alteration observed in the Santa Lúcia deposit. It exclusively affects the subvolcanic rock and is primarily represented by the selective, partial, or total replacement of igneous biotite by an early generation of chlorite (I). In this case, chlorite (I) generally retains the tabular form of the replaced biotite and display dark purple interference colors (**Fig. 6A**). Chlorite (I) veins and fracture infill are also commonly recognized (**Fig. 6B**). Clinozoisite aggregates and disseminated epidote (**Fig. 6C**) are common mineral phases associated with this alteration stage.

Potassic Alteration

Potassic alteration is poorly preserved at Santa Lúcia and spatially restricted to small-size (< 2 m) alteration fronts in the subvolcanic rock. It is represented by the formation of medium-grained (up to 1 cm), hydrothermal microcline, accompanied by subordinate quartz crystallization (**Fig. 6D**). Although relatively limited, this alteration is conspicuous in drill cores due to its intense reddish color, which is a result of microcline coating by microcrystalline hematite (**Fig. 6E**).

Greisen Alteration

Greisen alteration is widespread at Santa Lúcia and overprints the early chlorite-(epidote) and potassic alterations in the subvolcanic rock. The greisenization process is characterized by the replacement of igneous and hydrothermal potassium feldspar, and biotite, by a quartz-muscovite-tourmaline-rich assemblage (**Fig. 6F**). In this case, the alteration is marked by concomitant stages of muscovite and tourmaline (**Fig. 6G**), commonly aligned to the rock

foliation (**Fig. 6H**), accompanied by a significant increase in quartz. Thin (< 6 cm) tourmaline-muscovite alteration halos are generally observed at the contact zones between the pegmatite and the subvolcanic rock (**Fig. 6I**).

Chlorite (II) is also an important product of this alteration phase. Its timing relationship with muscovite in greisenized domains is, however, ambiguous. Although they appear to locally display equilibrium textures, marked by straight grain boundaries (**Fig. 6J**), incipient muscovite replacement by chlorite (II) is also commonly recognized, mainly along the muscovite cleavage planes (**Fig. 6K**). Milky quartz veins (< 5 cm thick) containing tourmaline aggregates, fine-grained muscovite crystals, chlorite (II) and minor chalcopyrite, are also associated with the greisenization process (**Fig. 6L**).

Copper-Gold Ore

The copper-gold ore at the Santa Lúcia deposit is chiefly represented by mineralized breccia bodies (**Fig. 7A**) of variable thickness (up to 6 m in drill cores), which are exclusively hosted by the subvolcanic rock (**Fig. 7B**) and enveloped by zones of significant muscovite- and tourmaline-enrichment (**Fig. 7C**). Less commonly, mineralization can occur in veinlets (**Fig. 8A**), disseminated (**Fig. 8B**) or associated with milky quartz veins. The breccias are predominantly matrix-supported, although clast-supported zones are locally recognized. Clasts are mainly derived from the host subvolcanic rock, previously affected by chlorite and potassic alteration, but commonly include milky quartz crystals (**Fig. 7D**). Both are generally angular to subrounded and range from < 0.3 to > 4 cm in diameter.

The ore breccia groundmass consists primarily of massive chalcopyrite (up to 75 vol% chalcopyrite; **Fig. 7E**), followed by sphalerite and pyrrhotite that are commonly associated with fluorapatite, quartz, muscovite, chlorite (II), carbonate, biotite, tourmaline and allanite (**Fig. 8C-G**). Sphalerite occurs as colloform (**Fig. 8H**) or acicular crystals, commonly exhibiting chalcopyrite exsolution features (chalcopyrite disease; **Fig. 8I**). Pyrrhotite usually forms xenoblastic crystals, which may contain fine-grained, pentlandite exsolutions along its rims (**Fig. 8J**). Pyrite occurs as idioblastic inclusions in sphalerite and chalcopyrite (**Fig. 8K**), and it may also form millimeter-sized veinlets that crosscut zones containing other sulfide minerals. Minor molybdenite (**Fig. 8L**) is also observed in the ore samples. Although most sulfides show no evidence of deformation, zones with high strained chalcopyrite, quartz and apatite are observed in places (**Fig. 7F**). (La-Ce-Nd)-monazite, Y-xenotime, melonite, Ce-bastnaesite, Te-bismuthite (**Fig. 8M**) and cassiterite (**Fig. 8N**) represent accessory phases that mostly occur as tiny inclusions in chalcopyrite and sphalerite.

Post-ore Veins and Fracture Infill

Post-ore hydrothermal activity at Santa Lúcia is represented by millimeter-size veinlets filled with fine-grained, greenish-to-yellowish sericite. These veinlets crosscut all previous zones of hydrothermal alteration and the pegmatite

intrusions (**Fig. 8O**), partially altering both igneous and hydrothermal potassium feldspar, as well as tourmaline crystals (**Fig. 8P**).

The latest hydrothermal stage recognized at Santa Lúcia corresponds to the formation of distinct hematite-rich zones. It is generally associated with fracture-controlled, millimeter-sized veinlets composed of microcrystalline hematite ± rutile, which appear to have preferentially developed over zones previously affected by potassic alteration (**Fig. 9A**). The hematite veinlets crosscut both the pegmatite and the subvolcanic rock, occurring commonly aligned to the rock foliation in the latter case (**Fig. 9B**). Hematite-rich zones are also recognized in breccia domains, in which hematite forms a fine-grained groundmass that involves extremely angular fragments of the subvolcanic rock (**Fig. 9C-D**). Paragenetic associations at Santa Lúcia are shown in **Figure 10**.

Ore Geochemistry

Trace elements and REE data of five samples from the main ore zone of the Santa Lúcia deposit are shown in **ESM Table 1** (Electronic Supplementary Material). In general, the ore is characterized by low to moderate (< 15 ppm) HFSE (Nb, Ta, Th, U, and Hf) contents, except for Zr that may exceed 100 ppm. In terms of LILE, the ore shows low Cs (0.07–0.29 ppm), low to moderate Sr (2.29–22.9 ppm), Rb (0.80–71.1 ppm) and moderate to high Ba (7.69–635 ppm) contents. Among transitional elements, the deposit demonstrates high contents of Cu (90824–230237 ppm), Zn (102–10544 ppm), Ni (169–3213 ppm) and Co (59.4–1954 ppm). Noteworthy, Cr contents are remarkably high at Santa Lúcia, ranging from 108 to 479 ppm, whereas concentrations of other metals, such as Bi and Mo, are generally moderate (few tens of ppm). Furthermore, the ore at Santa Lúcia shows moderate contents of Sn (up to 80 ppm) and very low (< 3 ppm) concentrations of W. However, one of the analyzed samples (FD22/73.45) contains more than 2500 ppm of tungsten, even though W-rich minerals, such as wolframite and scheelite, were not recognized during petrographic and SEM analyses.

The ore at Santa Lúcia is also characterized by significantly variable and high total REE contents, ($\sum_{ETR}$ = 1057–2538 ppm, **ESM Table 1**), except for one of the samples (FD22/74.05) that displays extremely low total REE concentrations ($\sum_{ETR}$ = 3.15 ppm). This can be attributed to the higher amount of quartz associated with mineralization in this case, over minerals such as apatite and monazite, which are the main carriers of REE in the ore assemblage. Nevertheless, no substantial differences in chondrite-normalized REE patterns (**Fig. 11**) were observed between the samples, which all show clear enrichment in LREE (La_N/Lu_N = 85.90–355.96) and prominent negative Eu anomalies (Eu/Eu* = 0.19–0.29).

Chemical and Boron Isotope Compositions of Tourmaline

Six tourmaline samples were selected for EMPA analyses and their chemical compositions are shown in **ESM Table 2**. Both pegmatite- and ore-related tourmaline are optically homogenous, with fractures commonly infilled by sericite (**Fig. 12A-E**). Tourmaline within the ore zones generally displays equilibrium textures with chalcopyrite and sphalerite (**Fig. 12F**). All the analyzed grains have low Ca contents (mostly below 0.1 a.p.f.u.) and plot in the alkali field (**Fig. 13A**), according to the classification of Henry et al. (2011), with X-site vacancies ranging from near-zero to 0.364 a.p.f.u. Contents of Cr_2O_3, V_2O_3, F, and Cl are low and commonly below detection limits. Oxide totals vary between ~ 84 and 89 wt.%. In the Al-Mg-Fe ternary plot of Henry and Guidotti (1985), the samples cluster in field 2 (lithium-poor granitoids, pegmatites, and aplites) of the Mg-poor side, evidencing a composition similar to schörl (**Fig. 13B**). This is also illustrated by the Ca / (Ca + Na) and Fe / (Fe + Mg) ratios, which range from 0.092 to 0.189 and 0.608 to 0.910, respectively (**Fig. 13C**). Both tourmaline generations plot along the schorl to dravite trend, falling approximately parallel to the $MgFe_{-1}$ exchange vector (**Fig. 13D**).

Tourmaline from the Santa Lúcia deposit has a narrow range of $\delta^{11}B$ values from -3.7 to -0.6‰ (n = 18; **Table 1** and **Fig. 12A-F**), with a mean value of -2.2‰. Tourmaline from the pegmatite body yielded $\delta^{11}B$ values spanning from -3.7 to -1.7‰ (n = 10), whereas tourmaline associated with the brecciated ore zone displayed slightly higher $\delta^{11}B$ values between -2.0 and -0.6‰ (n = 8). All the analyzed samples showed no internal zonation under transmitted light or backscattered images, and no significant isotopic variation between core and rim was evidenced.

SHRIMP II U-Pb Results

Monazite crystals from the main brecciated ore zone of the Santa Lúcia deposit are fine- to coarse-grained (few ten microns to > 1 mm), white to light yellow in thin section, subhedral to euhedral, and display either prismatic shape with pyramid terminations (**Fig. 14A**), or ovoid shape with rounded boundaries (**Fig.14B**). They occur predominantly as fine-grained inclusions in apatite, commonly forming aggregates (**Fig. 14C**). Coarse-grained prismatic crystals may show equilibrium textures with chalcopyrite, sphalerite, and pyrrhotite (**Fig. 14D**). No corrosion textures or internal structures were observed in BSE images (**Fig. 14E-H**).

A total of 16 spots were analyzed in sixteen monazite grains from sample FD022/80.10 (**Table 2**). Seven monazite grains yielded a concordant data (up to 10% discordant), from which five analyses clustered within a single population with a weighted average $^{207}Pb/^{206}Pb$ age of 2688 ± 27 Ma (MSWD = 0.14), whereas two grains provided younger ages of 2497 ± 40 Ma and 2071 ± 49 Ma, respectively (**Fig. 15**). All these grains displayed very low Th/U ratios, between 0.022 and 0.048. Seven discordant monazite grains displayed unreliable ages due to extreme Pb loss.

Discussion

Hydrothermal evolution of the Santa Lúcia deposit

The Santa Lúcia deposit displays similar hydrothermal alteration stages to those described in granite-related deposits of the CMP. The evolution of its hydrothermal system is marked by an early event of chlorite alteration, followed by potassic and greisen alteration stages that are interpreted to be genetically associated with the emplacement of the pegmatite body in the deposit area. The identification of ductile-brittle fabrics in the pegmatite, suggests that its emplacement was probably structurally controlled and may have occurred during a transition from ductile to brittle deformation regimes.

The greisenization at Santa Lúcia is mainly characterized by the development of a quartz-muscovite-tourmaline-rich assemblage that replaces the feldspars and the chloritized biotite in the subvolcanic rock. The term greisenization is generally applied to describe a late-magmatic metasomatic process that gives rise to leucocratic rocks (70-75% of SiO_2) due to the destabilization of biotite and feldspars of an igneous protolith, with consequent remobilization of silica and alumina (Stemprok 1987). Moreover, greisen-like alteration assemblages are generally developed by high-temperature (250º to 450ºC; Stemprok 1987), volatile-rich acidic fluids (Shcherba 1970). Hence, the recognition of muscovite- and tourmaline-rich alteration halos in the contact zones between the pegmatite intrusions and the subvolcanic rock, suggest a metasomatic process triggered by a boron-rich volatile phase. A similar alteration pattern has been recognized in the Estrela (Volp 2005) and Breves (Tallarico et al. 2004) deposits, although there are divergences among authors regarding the usage of the term greisenization for the latter. Based on the poorly-evolved nature of the granitic system, in addition to mineralogical and geochemical aspects of the Breves deposit, Botelho et al. (2005) have reinterpreted the greisenization event described by Tallarico et al. (2004) and alternatively proposed a stage of phengite-chlorite alteration.

Potassic alteration with microcline is also recognized at Santa Lúcia and could represent an evolutionary stage of the greisenization process. Pollard (1983) and Stemprok (1987) argue that a microcline stage commonly precedes the greisen alteration, as a consequence of fluids separated from a residual granitic melt. The destabilization of biotite and both igneous and hydrothermal microcline during the greisenization is, therefore, evidence of fluid evolution towards increasing acidity. This process has probably resulted from a decrease in the alkali/H^+ ratios of the hydrothermal system, which consequently led to the precipitation of quartz and muscovite. It is noteworthy that, chlorite growth may be facilitated under these relatively low pH conditions (Stemprok 1987). This would explain the incipient alteration of muscovite crystals by chlorite (II) in the deposit. Moreover, acidic conditions must have prevailed even after ore precipitation, as evidenced by the formation of late sericite veinlets and the destabilization of tourmaline from the pegmatite.

Hematite formation represents the latest stage of hydrothermal activity observed at Santa Lúcia, which developed under a dominantly brittle deformation regime. According to Pirajno (2009), hematite dissemination and vein

formation are commonly associated with the late hydrothermal stages in greisen-affiliated deposits, mainly due to the opening of the system to oxidizing meteoric fluids. In fact, the recognition of hydrolytic alteration assemblages with hematite and sericite in several other copper-gold deposits of the Southern Copper Belt, such as the Alvo 118, Bacaba, Bacuri and Sossego-Sequeirinho IOCG deposits (Monteiro et al. 2008; Moreto et al. 2011; Torresi et al. 2012; Melo et al. 2014), could indicate that such oxidizing fluids have broadly migrated through regional-scale structures.

Precipitation of massive chalcopyrite is conspicuous in the main breccia-hosted ore zone of the Santa Lucia deposit. These ore breccias are spatially associated with greisen-altered domains and may locally contain highly strained minerals, which could be an indication of continued deformation during mineralization. Although the physicochemical conditions responsible for the ore genesis are still uncertain, due to the lack of microthermometric data for the deposit, the sequence of hydrothermal events, combined with their correspondent mineral assemblages, suggest a progressive temperature drop of the system, whereas the pH remained acidic (i.e., late sericite formation). Although copper tends to remain in solution under low pH conditions, a considerable temperature decrease probably represented the main mechanism that triggered the precipitation of chalcopyrite (Liu and McPhail 2005).

Geochemical ore signature and implications for the metallogenesis of granite-related systems at Carajás

In general, the granite-related copper-gold deposits of the CMP are characterized by geochemical ore signatures with anomalous contents of granitophile elements, especially Sn, Bi, W, and Mo (Tallarico et al. 2004; Grainger et al. 2008). The ICP-MS analyses conducted in this study have revealed that the concentrations of these elements in the main ore zone of the Santa Lúcia are moderate (< 100 ppm) and compatible with data from mineralized bodies of the Breves deposit (Botelho et al. 2005). Additionally, the ore also shows strong enrichment in LREE, which is characteristic of the copper-gold systems of the Carajás Domain, especially those formed in the Neoarchean (Xavier et al. 2012, 2017).

Despite all these facts, one of the most remarkable features of the Santa Lúcia ore breccias is their surprisingly high Ni (> 3000 ppm), Co (~ 1900 ppm) and Cr (~ 500 ppm) contents, which appears to be a distinctive characteristics that sets it apart from other granite-related deposits, such as Breves. One possible explanation for this Ni-Co-Cr enrichment may be the specific geological setting of the Santa Lúcia deposit. Regional circulation of hydrothermal fluids that had previously interacted with mafic-ultramafic sequences in the surrounding areas of the deposit (e.g., Santa Inês Gabbro, Vermelho Complex), could represent a major factor governing the elevated concentrations of these transition elements at Santa Lúcia. In addition, Ni, Co and Cr may have also been leached from lenses of metamorphosed ultramafic rocks contained within felsic host rocks of the Neoarchean (ca. 2.7 Ga) Visconde (Silva et al. 2015) and Sequeirinho (Pista orebody; Monteiro et al. 2008) IOCG deposits in the Southern Copper Belt. Nevertheless, further studies should be conducted to investigate and confirm these hypotheses.

Tourmaline compositions and sources of boron at Santa Lúcia

Tourmaline from the pegmatite and the breccia ore zone of the Santa Lúcia deposit fall into the alkali group and within the schorl field, displaying no substantial compositional variations. Both tourmaline generations have total Al contents sufficient to account for full six cations in the Z site (> 6 a.p.f.u.; **ESM Table 2**). Thus, a significant substitution of Al by Fe^{3+} is unlikely to have occurred (Jiang et al. 2002; Henry et al. 2008). Conversely, the negative correlation between Fe (a.p.f.u.) and Mg (a.p.f.u.), with all data plotting roughly parallel to the $MgFe_{-1}$ exchange vector (**Fig. 13D**), suggests that the main mechanism of Mg incorporation into tourmaline was by substitution of Fe^{2+} in the Y site (Henry et al. 2008). Therefore, and considering the hydrothermal evolution of the Santa Lúcia deposit, the relative increment of Mg contents, in detriment of Fe, demonstrated by tourmaline from mineralized zones, indicates that the hydrothermal fluids were more reducing, with considerably lower concentrations of Fe^{3+} (Jiang et al. 2002).

Tourmaline from the Santa Lúcia deposit has boron isotopic compositions between -3.7 to -0.6‰. Based on the potential boron reservoirs (Barth 1993; Marschall and Jiang 2011), the homogeneous and negative $\delta^{11}B$ values are compatible with a magmatic boron source within the range reported for granite and pegmatite (**Fig. 16**). The small, but significant, shift of boron isotope values in tourmaline from the pegmatite (-3.7 to -1.7‰) to those in the ore zones (-2.0 to -0.6‰) may be linked to fractionation due to temperature decrease (Meyer et al. 2008; Marschall et al. 2009).

Notably, our data also overlap the range of $\delta^{11}B$ values obtained for tourmaline of the Breves deposit (-3.6 to 1.8‰), which combined with hydrogen isotope data (δD = -116 to -99‰) is attributed to magmatic fluid sources (Xavier et al. 2013). However, it is important to point out that Cl/Br and Na/Cl ratios recorded in inclusion fluids at Breves indicate a contribution of bittern fluids to the hydrothermal system (Xavier et al. 2009).

Timing of ore formation and implications for the Cu-Au metallogeny of the Carajás Domain

Hydrothermal monazite grains within the main brecciated ore zone of the Santa Lúcia deposit yielded a weighted average $^{207}Pb/^{206}Pb$ age of 2688 ± 27 Ma (MSWD = 0.14). The low Th/U ratios displayed by these grains, coupled with the ore paragenesis, with monazite restricted to chalcopyrite-sphalerite-pyrrhotite-rich zones, indicate that this age reflects the main mineralization event at the deposit.

The Santa Lúcia deposit shares several similarities with the granite-related Cu-Au-(W-Bi-Sn) deposits of the Carajás Domain. These deposits are regarded as typical shallow hydrothermal systems whose genesis has been particularly associated with the widespread Paleoproterozoic (ca. 1.88 Ga) A-type granitic magmatism event recorded in the Carajás Domain. The SHRIMP II U-Pb dating on zircon, monazite and xenotime crystals of the Breves deposit placed the age of copper-gold mineralization at ca. 1.88–1.87 Ga (Tallarico et al. 2004). Similarly, ore precipitation at Estrela was coeval with the emplacement of granitic intrusions at ca. 1.88 Ga (Lindenmayer et al. 2005), whereas

a genetic link between the emplacement of the Serra dos Carajás granite in the Águas Claras deposit area (ca. 1.88 Ga; Machado et al. 1991), and ore genesis, is suggested by Sm-Nd and Pb-Pb geochronological data (Mougeot et al. 1996; Silva and Villas 1998). Hence, our data clearly attest that the Santa Lúcia deposit is so far the first iron oxide-poor, copper-gold deposit formed during the Neoarchean in the Carajás Domain. Therefore, the deposit has likely formed at the same metallogenetic epoch (ca. 2.72–2.68 Ga) that generated a broad group of IOCG deposits in the Southern Copper Belt, including the Sequeirinho orebody at the Sossego deposit and the Bacaba, Bacuri and Visconde deposits (Moreto et al. 2015a, b; Silva et al. 2015).

Hydrothermal alteration (i.e., greisenization) and copper-gold mineralization appears to be both spatially and temporally associated with pegmatite emplacement at Santa Lúcia. Despite lacking geochronological data, the pegmatite body recognized in the deposit area may be regionally linked with the widespread ca. 2.7 Ga Planalto Granite Suite, along the Canaã Shear Zone. Although a crystallization age between 2740 and 2730 Ma has been proposed for this unit (Feio et al. 2013), younger U-Pb LA-MC-ICP-MS zircon ages (2729 ± 17 Ma, 2710 ± 10 Ma, 2706 ± 5 Ma; Feio et al. 2012) are also documented and overlap within error of the mineralization age obtained in this study. According to Moreto et al. (2015a, b), these younger ages of the Planalto Granite Suite are similar to those of the Neoarchean IOCG-forming system in the Southern Copper Belt (2.72–2.68 Ga), and could possibly imply a magmatic origin for the mineralizing fluids. In this sense, monazite crystallization within the ore zones of the Santa Lúcia deposit could also have been synchronous and genetically correlated with a Neoarchean episode of granite magmatism. This is further corroborated by the boron isotope compositions of tourmaline ($\delta^{11}B$ = -3.7 to -0.6‰), which clearly indicate a magmatic source for boron, and possibly for the ore-forming fluids. However, little is known about a significant granite magmatism event at 2.72–2.68 in the Carajás Domain, as well as its possible implications on the genesis of IOCG and granite-related deposits, especially in the Southern Copper Belt. Additionally, although there is much evidence supporting that the Santa Lúcia deposit evolved fundamentally in the Neoarchean, a Paleoproterozoic age for the pegmatite cannot be completely ruled out. If this scenario is considered, the deposit would have registered the overprinting of a Paleoproterozoic granite magmatism event over a previously established Neoarchean, non-IOCG system.

Nevertheless, the 2688 ± 27 Ma mineralization age presented here is not only important for the understanding of the origin of granite-related copper-gold systems in the Carajás Domain, but also for the genesis of synchronous IOCG deposits. Indeed, the existence of magmatic-hydrothermal systems at ca. 2.7 Ga may explain the participation of magmatic fluids in the evolution of several IOCG deposits located in Southern Copper Belt, as indicated by fluid inclusion and stable isotope data at Sossego, Castanha and Visconde (Chiaradia et al. 2006; Monteiro et al. 2008; Pestilho 2011; Silva et al. 2015).

Conclusions

The Santa Lúcia deposit lithotypes and hydrothermal alteration patterns, combined with the geochemical and geochronological data obtained in this study, provide a better understanding of the evolution of its hydrothermal system:

1. A variably mylonitized and hydrothermally altered subvolcanic rock of rhyolitic composition represents the deposit host rocks. This unit, which has been correlated to the Grão Pará Group, is intersected by relatively undeformed pegmatite intrusions.
2. The sequence of hydrothermal alteration stages recognized at Santa Lúcia comprises (1) an early chloritization, followed by (2) potassic alteration with microcline, (3) intense greisenization, with quartz, muscovite and tourmaline precipitation, (4) copper-gold mineralization, and (5) late sericite and hematite vein formation and fracture infilling.
3. Breccia-hosted ore bodies comprise the main style of copper-gold mineralization identified in the deposit. They are spatially associated with greisen-altered domains and characterized by a relatively reduced ore assemblage composed of chalcopyrite, sphalerite, pyrrhotite, pentlandite, and pyrite, with minor molybdenite, REE-bearing phases, tellurobismuthite, and cassiterite. This ore paragenesis is consistent with that presented by the Paleoproterozoic (ca. 1.88 Ga) granite-related copper-gold systems of Carajás, including Breves and Estrela.
4. The geochemical ore signature of the Santa Lúcia ore breccias points to a significant Ni, Co and Cr enrichment, which could have been leached from ultramafic rocks present in surrounding areas of the deposit or associated with Neoarchean (ca. 2.7 Ga) IOCG systems in the Southern Copper Belt. Additionally, concentrations of granitophile elements (e.g., Sn, Bi, W, and Mo) are compatible with those shown by other granite-related deposits of the CMP.
5. Tourmaline from the Santa Lúcia deposit have a schorlitic composition with $\delta^{11}B$ values ranging from -3.7 to -0.6‰, which fall within the known range for magmatic boron sources.
6. Monazite from the ore breccias yielded a weighted average $^{207}Pb/^{206}Pb$ age of 2688 ± 27 Ma (MSWD = 0.14). This age, combined with the geological attributes and geochemical signatures of the Santa Lúcia deposit point to the genesis of a magmatic-hydrothermal system in the Neoarchean, due to coeval A-type granite magmatism.
7. These results indicate that the 2.72–2.68 Ga metallogenetic event responsible for the genesis of important IOCG deposits, especially in the Southern Copper Belt, should also be extended for the formation of copper-gold systems without significant iron oxide content.

Acknowledgments We are immensely grateful to VALE for their unceasing support, especially to geologists Fernando Matos and Samuel Nunes. We also thank Peter J. Pollard and Fernando Tornos for their constructive reviews and insightful suggestions that greatly improved the quality of this manuscript, as well as the editorial handling by Steffen Hagemann and Georges Beaudoin. The fieldwork was funded by the INCT Geociências da Amazônia (MCT/CNPq/Fapespa 573733/2008-2). This research was only made possible by the institutional partnerships established between UNICAMP and Wuhan University of Technology, China University of Geosciences and Curtin University of Technology.

References

Araújo OJB, Maia RGN, Jorge-João XS, Costa JBS (1988) A megaestruturação da folha Serra dos Carajás. In: VII Congresso Latino-Americano de Geologia. Belém, pp 324–333

Avelar VG, Lafon JM, Correia Jr. FC, Macambira EMB (1999) O magmatismo arqueano da região de Tucumã - Província Mineral De Carajás: Novos resultados geocronológicos. Rev Bras Geociências 29:453–460

Barros CEM, Macambira MJB, Barbey P, Scheller T (2004) Dados isotópicos Pb-Pb em zircão (evaporação) e Sm-Nd do Complexo Granítico Estrela, Província Mineral de Carajás, Brasil: Implicações petrológicas e tectônicas. Rev Bras Geociências 34:531–538

Barros CEM, Sardinha AS, Macambira MJB et al (2009) Structure, petrology, geochemistry and zircon U/Pb and Pb/Pb geochronology of the synkinematic archean (2.7 Ga) A-type granites from the Carajás Metallogenetic Province, northern Brazil. Can Mineral 47:1423–1440. https://doi:10.3749/canmin.47.6.1423

Barth S (1993) Boron isotope variations in nature: a synthesis. Geol Rundschau 82:640–651. https://doi:10.1007/BF00191491

Botelho NF, Moura MA, Teixeira LM et al (2005) Caracterização geológica e metalogenética do depósito de Cu ± (Au, W, Mo, Sn) Breves, Carajás. In: Marini OJ, Queiroz ET, Ramos BW (eds) Caracterização de depósitos minerais em distritos mineiros da Amazônia. DNPM/CT-Mineral/ADIMB, Brasília, pp 335–389

Chiaradia M, Banks D, Cliff R et al (2006) Origin of fluids in iron oxide-copper-gold deposits: Constraints from δ37Cl, 87Sr/86Sr and Cl/Br. Miner Depos 41:565–573. https://doi:10.1007/s00126-006-0082-6

Costa UAP, Paula RR, Silva DPB et al (2016) Programa Geologia do Brasil-PGB – Mapa de integração geológico-geofísica da ARIM Carajás. Escala 1:250.000. CPRM, Belém

Dardenne MA, Ferreira Filho CF, Meirelles MR (1988) The role of shoshonitic and calc-alkaline suites in the tectonic evolution of the Carajás District, Brazil. J South Am Earth Sci 1:363–372. https://doi:10.1016/0895-9811(88)90023-5

DOCEGEO (1988) Revisão litoestratigráfica da Província Mineral de Carajás - Litoestratigrafia e principais depósitos minerais. In: XXXV Congresso Brasileiro de Geologia. SBG, Belém, pp 11–54

DOCEGEO (2002) Projeto Serra do Rabo - Alvo Estrela. Rio Doce Geologia e Mineração S/A Internal Report

Feio GRL, Dall'Agnol R, Dantas EL et al (2013) Archean granitoid magmatism in the Canaã dos Carajás area: Implications for crustal evolution of the Carajás province, Amazonian craton, Brazil. Precambrian Res 227:157–185. https://doi:10.1016/j.precamres.2012.04.007

Feio GRL, Dall'Agnol R, Dantas EL et al (2012) Geochemistry, geochronology, and origin of the Neoarchean Planalto Granite suite, Carajás, Amazonian craton: A-type or hydrated charnockitic granites? Lithos 151:57–73. https://doi:10.1016/j.lithos.2012.02.020

Ferreira Filho CF, Cançado F, Correa C et al (2007) Mineralizações estratiformes de PGE-Ni associadas a complexos acamadados em Carajás: os exemplos de Luanga e Serra da Onça. In: Rosa-Costa LT, Klein EL, Viglio EP (eds) Contribuições à geologia da Amazônia, v. 5. SBG-Núcleo Norte, Belém, pp 1–14

Fletcher IR, McNaughton NJ, Davis WJ, Rasmussen B (2010) Matrix effects and calibration limitations in ion probe U-Pb and Th-Pb dating of monazite. Chem Geol 270:31–44. https://doi: 10.1016/j.chemgeo.2009.11.003

Grainger CJ, Groves DI, Tallarico FHB, Fletcher IR (2008) Metallogenesis of the Carajás Mineral Province, Southern Amazon Craton, Brazil: Varying styles of Archean through Paleoproterozoic to Neoproterozoic base- and precious-metal mineralisation. Ore Geol Rev 33:451–489. https://doi:10.1016/j.oregeorev.2006.10.010

Henry DJ, Dutrow BL (1996) Metamorphic tourmaline and its petrologic applications. In: Grew ES, Anovitz LM (eds) Boron: Mineralogy, Petrology and Geochemistry, 33rd edn. Mineralogical Society of America. Reviews in Mineralogy, pp 503–558

Henry DJ, Guidotti CV (1985) Tourmaline as a petrogenetic indicator mineral: an example from the staurolite-grade metapelites of NW Maine. Am Mineral 70:1–15

Henry DJ, Novák M, Hawthorne FC et al (2011) Nomenclature of the tourmaline-supergroup minerals. Am Mineral 96:895–913. https://doi:10.2138/am.2011.3636

Henry DJ, Sun H, Slack JF, Dutrow BL (2008) Tourmaline in meta-evaporites and highly magnesian rocks: perspectives from Namibian tourmalinites. Eur J Mineral 20:889–904. https://doi:10.1127/0935-1221/2008/0020-1879

Hirata WK, Rigon JC, Kadekaru K et al (1982) Geologia regional da Província Mineral de Carajás. In: I Simpósio de Geologia da Amazônia. SBG/NO, Belém, pp 100–110

Hou KJ, Li YH, Xiao YK et al (2010) In situ boron isotope measurements of natural geological materials by LA-MC-ICP-MS. Chinese Sci Bull 55:3305–3311. https://doi:10.1007/s11434-010-4064-9

Huhn SRB, Macambira MJB, Dall'Agnol R (1999) Geologia e geocronologia Pb-Pb do Granito Alcalino Planalto, Região da Serra do Rabo, Carajás-PA. In: VI Simpósio de Geologia da Amazônia. SBG-Núcleo Norte, pp 463–466

Hunger RB, Xavier RP, Moreto CPN, Gao J-F (2018) Hydrothermal Alteration, Fluid Evolution, and Re-Os Geochronology of the Grota Funda Iron Oxide Copper-Gold Deposit, Carajás Province (Pará State), Brazil. Econ Geol 113:1769–1794. https://doi:10.5382/econgeo.2018.4612

Jiang SY, Palmer MR, Yeats CJ (2002) Chemical and boron isotopic compositions of tourmaline from the Archean Big Bell and Mount Gibson gold deposits, Murchison Province, Yilgarn Craton, Western Australia. Chem Geol 188:229–247. https://doi.org/10.1016/S0009-2541(02)00107-9

Lima FD (2002) Evolução Tectônica da Terminação Leste da Falha Carajás, Sul do Estado do Pará. Dissertation, Universidade Federal do Pará

Lima FD, Pinheiro RVL (1999) As rochas mesoproterozóicas na terminação leste da Falha Carajás, Serra dos Carajás, Estado do Pará. In: VI Simpósio de Geologia da Amazônia. SBG-NO, Manaus, pp 274–277

Lindenmayer ZG, Fleck A, Gomes CH et al (2005) Caracterização geológica do Alvo Estrela (Cu-Au), Serra dos Carajás, Pará. In: Marini OJ, Queiroz ET, Ramos BW (eds) Caracterização de depósitos minerais em distritos mineiros da Amazônia. DNPM/CT-Mineral/ADIMB, Brasília, pp 153–226

Lindenmayer ZG, Pimentel MM, Ronchi LH et al (2001) Geologia do depósito de Cu-Au de Gameleira, Serra dos Carajás, Pará. In: Jost H, Brod JA, Queiroz ET (eds) Caracterização de depósitos auríferos em distritos mineiros. DNPM/ADIMB, Brasília, pp 81–139

Liu W, McPhail DC (2005) Thermodynamic properties of copper chloride complexes and copper transport in magmatic-hydrothermal solutions. Chem Geol 221:21–39. https://doi:10.1016/j.chemgeo.2005.04.009

Lobato LM, Rosière CA, Silva RCF et al (2005) A mineralização hidrotermal de ferro da Província Mineral de Carajás: Controle estrutural e contexto na evolução metalogenética da província. In: Marini OJ, Queiroz ET, Ramos BW (eds) Caracterização de depósitos minerais em distritos mineiros da Amazônia. DNPM/CT-Mineral/ADIMB, Brasília, pp 21–92

Ludwig KR (2003) User's manual for Isoplot 3.0. In: A Geochronological Toolkit for Microsoft Excel. BGC Special Publication No. 4, Berkeley, pp 4–71

Macambira EMB, Ferreira Filho CF (2002) Fracionamento magmático dos corpos máfico-ultramáficos da Suíte Intrusiva Cateté – sudeste do Pará. In: Klein EL, Vasquez ML, Rosa-Costa LT (eds) Contribuições à geologia da Amazônia, v. 3. SBG-Núcleo Norte, Belém, pp 105–114

Macambira EMB, Vale AG (1997) São Félix do Xingu: folha SB.22-Y-B, Estado do Pará, escala 1:250.000. Texto Explicativo. In: Programa Levantamentos Geológicos Básicos do Brasil (PLGB). CPRM, Brasília, p 344

Machado N, Lindenmayer Z, Krogh TE, Lindenmayer D (1991) U-Pb geochronology of Archean magmatism and basement reactivation in the Carajás area, Amazon shield, Brazil. Precambrian Res 49:329–354. https://doi: 10.1016/0301-9268(91)90040-H

Marschall HR, Jiang SY (2011) Tourmaline isotopes: No element left behind. Elements 7:313–319. https://doi: 10.2113/gselements.7.5.313

Marschall HR, Meyer C, Wunder B et al (2009) Experimental boron isotope fractionation between tourmaline and fluid: Confirmation from in situ analyses by secondary ion mass spectrometry and from Rayleigh fractionation modelling. Contrib to Mineral Petrol 158:675–681. https://doi:10.1007/s00410-009-0403-8

Meirelles MR (1986) Geoquímica e petrologia dos jaspilitos e rochas vulcânicas associadas, Grupo Grão-Pará, Serra dos Carajás. Dissertation, Universidade de Brasília

Meirelles MR, Dardenne MA (1991) Vulcanismo basáltico de afinidade shoshonítica em ambiente de arco arqueano, Grupo Grão-Pará, Serra Dos Carajás - Pará. Rev Bras Geociências 21:41–50

Melo GHC, Monteiro LVS, Moreto CPN et al (2014) Paragenesis and evolution of the hydrothermal Bacuri iron oxide-copper-gold deposit, Carajás Province (PA). Brazilian J Geol 44:73–90. https://doi:10.5327/Z2317-4889201400010007

Melo GHC, Monteiro LVS, Xavier RP et al (2019) Tracing Fluid Sources for the Salobo and Igarapé Bahia Deposits: Implications for the Genesis of the Iron Oxide Copper-Gold Deposits in the Carajás Province, Brazil. Econ Geol 114:697–718. https://doi:10.5382/econgeo.4659

Melo GHC, Monteiro LVS, Xavier RP et al (2016) Temporal evolution of the giant Salobo IOCG deposit, Carajás Province (Brazil): Constraints from paragenesis of hydrothermal alteration and U-Pb geochronology. Miner Depos 52:709–732. https://doi:10.1007/s00126-016-0693-5

Meyer C, Wunder B, Meixner A et al (2008) Boron-isotope fractionation between tourmaline and fluid: An experimental re-investigation. Contrib to Mineral Petrol 156:259–267. https://doi:10.1007/s00410-008-0285-1

Monteiro LVS, Xavier RP, Carvalho ER et al (2008) Spatial and temporal zoning of hydrothermal alteration and mineralization in the Sossego iron oxide–copper–gold deposit, Carajás Mineral Province, Brazil: paragenesis and stable isotope constraints. Miner Depos 43:129–159. https://doi:10.1007/s00126-006-0121-3

Moreto CPN, Monteiro LVS, Xavier RP et al (2015a) Neoarchean and paleoproterozoic iron oxide-copper-gold events at the Sossego deposit, Carajás Province, Brazil: Re-Os and U-Pb geochronological evidence. Econ Geol 110:809–835. https://doi:10.2113/econgeo.110.3.809

Moreto CPN, Monteiro LVS, Xavier RP et al (2015b) Timing of multiple hydrothermal events in the iron oxide–copper–gold deposits of the Southern Copper Belt, Carajás Province, Brazil. Miner Depos 50:517–546. https://doi:10.1007/s00126-014-0549-9

Moreto CPN, Monteiro LVS, Xavier RP et al (2011) Mesoarchean (3.0 and 2.86 Ga) host rocks of the iron oxide-Cu-Au Bacaba deposit, Carajás Mineral Province: U-Pb geochronology and metallogenetic implications. Miner Depos 46:789–811. https://doi:10.1007/s00126-011-0352-9

Mougeot R, Respaut JP, Brique L et al (1996) Geochronological constraints for the age of the Águas Claras Formation (Carajás Province, Pará, Brazil). In: XXXIX Congresso Brasileiro de Geologia. SBG, Salvador, pp 579–581

Nogueira ACR, Truckenbrodt W, Pinheiro RVL (1995) Formação Águas Claras, Pré-Cambriano da Serra dos Carajás: Redescrição e redefinição litoestratigráfica. Bol do Mus Para Emílio Goeldi - Série Ciências da Terra 7:177–277

OZ Minerals (2019) ASX Release – Carajás Hub strategy gains pace. https://www.ozminerals.com/media/carajas-hub-strategy-gains-pace/. Accessed 22 January 2020

Pestilho ALS (2011) Sistemática de isótopos estáveis aplicada à caracterização da evolução dos paleo-sistemas hidrotermais associados aos depósitos cupríferos Alvo Bacaba e Alvo Castanha, Província Mineral de Carajás, PA. Dissertation, University of Campinas

Pinheiro RVL (1997) Reactivation history of the Carajás and Cinzento strike-slip systems, Amazon, Brazil. Thesis, Durham University

Pinheiro RVL, Holdsworth RE (2000) Evolução tectonoestratigráfica dos sistemas transcorrentes Carajás e Cinzento, Cinturão Itacaiúnas, na borda leste do Cráton Amazônico,Pará. Rev Bras Geociências 30:597–606

Pirajno F (2009) Hydrothermal processes and mineral systems. Springer Netherlands, Dordrecht

Pollard PJ (1983) Magmatic and postmagmatic processes in the formation of rocks associated with rare-element deposits. Trans Inst Min Metall 92: B1-B9

Pollard PJ, Taylor RG, Peters L et al (2019) 40Ar-39Ar dating of Archean iron oxide Cu-Au and Paleoproterozoic granite-related Cu-Au deposits in the Carajás Mineral Province, Brazil: implications for genetic models. Miner Depos 54:329–346. https://doi:10.1007/s00126-018-0809-1

Ricci PSF, Carvalho MA (2006) Rocks of the Pium-area, Carajás Block, Brazil - A deep seated high-T abbroic pluton (charnockitoid-like) with xenoliths of enderbitic gneisse dated at 3002 Ma - The basement problem revisited. In: VIII Simpósio de Geologia da Amazônia. SBG, Belém, p [CD ROM]

Rodrigues DS, Oliveira DC, Macambira MJB (2014) Geologia, geoquímica e geocronologia do Granito Mesoarqueano Boa Sorte, município de Água Azul do Norte, Pará – Província Carajás. Bol do Mus Para Emílio Goeldi - Série Ciências Nat 9:597–633

Sardinha AS, Barros CEM, Krymsky R (2006) Geology, geochemistry, and U-Pb geochronology of the Archean (2.74 Ga) Serra do Rabo granite stocks, Carajás Metallogenetic Province, northern Brazil. J South Am Earth Sci 20:327–339. https://doi:10.1016/j.jsames.2005.11.001

Shcherba GN (1970) Greisens. Int Geol Rev 12:114–150. https://doi:10.1080/00206817009475216

Silva ARC, Villas RNN, Lafon J-M et al (2015) Stable isotope systematics and fluid inclusion studies in the Cu–Au Visconde deposit, Carajás Mineral Province, Brazil: implications for fluid source generation. Miner Depos 50:547–569. https://doi:10.1007/s00126-014-0558-8

Silva CMG, Villas RN (1998) The Águas Claras Cu-sulfide ± Au deposit, Carajás region, Pará, Brazil: Geological setting, wall-rock alteration and mineralizing fluids. Rev Bras Geociências 28:315–326

Silva MG, Teixeira JBG, Pimentel MM et al (2005) Geologia e mineralizações de Fe-Cu-Au do Alvo GT46 (Igarapé Cinzento), Carajás. In: Marini OJ, Queiroz ET, Ramos BW (eds) Caracterização de depósitos minerais em distritos mineiros da Amazônia. DNPM/CT-Mineral/ADIMB, Brasília, pp 94–151

Soares AD V., Santos AB, Vieira A et al (1994) Área Águas Claras: Contexto geológico e mineralizações. In: IV Simpósio de Geologia da Amazônia. SBG, Belém, pp 379–382

Souza SRB, Macambira MJB, Sheller T (1996) Novos dados geocronológicos para os granitos deformados do Rio Itacaiúnas (Serra dos Carajás, PA): implicações estratigráficas. In: V Simpósio de Geologia da Amazônia. SBG, Belém, pp 380–383

Stemprok M (1987) Greisenization (a review). Geol Rundschau 76:169–175. https://10.1007/BF01820580

Tallarico FHB (2003) O cinturão cupro-aurífero de Carajás, Brasil. Thesis, Universidade Estadual de Campinas

Tallarico FHB, Figueiredo BR, Groves DI et al (2005) Geology and SHRIMP U-Pb geochronology of the Igarapé Bahia deposit, Carajás copper-gold belt, Brazil: An Archean (2.57 Ga) example of Iron-Oxide Cu-Au-(U-REE) mineralization. Econ Geol 100:7–28. https://doi:10.2113/100.1.0007

Tallarico FHB, McNaughton NJ, Groves DI et al (2004) Geological and SHRIMP II U-Pb constraints on the age and origin of the Breves Cu-Au-(W-Bi-Sn) deposit, Carajás, Brazil. Miner Depos 39:68–86. https://doi:10.1007/s00126-003-0383-y

Tassinari CCG (1996) O mapa geocronológico do Cráton Amazônico no Brasil: revisão dos dados isotópicos. Thesis, University of São Paulo

Tassinari CCG, Macambira MJB (2004) A evolução tectônica do Craton Amazônico. In: Mantesso-Neto V, Bartorelli A, Carneiro CDR, Brito Neves BB (eds) Geologia do Continente Sul-Americano: Evolução da obra de Fernando Flávio Marques Almeida. Beca, São Paulo, pp 471–485

Tassinari CCG, Macambira MJB (1999) Geochronological provinces of the Amazonian Craton. Episodes 22:174–182. https://doi:10.1080/00206819709465329

Tavares FM, Trouw RAJ, da Silva CMG et al (2018) The multistage tectonic evolution of the northeastern Carajás Province, Amazonian Craton, Brazil: Revealing complex structural patterns. J South Am Earth Sci 88:238–252. https://doi:10.1016/j.jsames.2018.08.024

Teixeira JBG (1994) Geochemistry, petrology, and tectonic setting of the archean basaltic and dioritic rocks from the N4 Iron deposit, Serra dos Carajás, Pará, Brazil. Thesis, Penn State University

Teixeira JBG, Lindenmayer ZG, Silva MG (2010) Depósitos de Óxido de Fe, Cu-Au de Carajás. In: Brito RSC, Silva MG, Kuyumjian RM (eds) Modelos de depósitos de cobre do Brasil e sua resposta ao intemperismo, 1 ed. CPRM, Brasília, pp 15–48

Teixeira W, Tassinari CCG, Cordani UG, Kawashita K (1989) A review of the geochronology of the Amazonian Craton: Tectonic implications. Precambrian Res 42:213–227. https://doi:10.1016/0301-9268(89)90012-0

Toledo PI de F, Moreto CPN, Xavier RP et al (2019) Multistage Evolution of the Neoarchean (ca. 2.7 Ga) Igarapé Cinzento (GT-46) Iron Oxide Copper-Gold Deposit, Cinzento Shear Zone, Carajás Province, Brazil. Econ Geol 114:1–34. https://doi:10.5382/econgeo.2019.4617

Tonarini S, Pennisi M, Adorni-Braccesi A et al (2003) Intercomparison of boron isotope and concentration measurements. Part I: Selection, preparation and homogeneity tests of the intercomparison materials. Geostand Newsl 27:21–39. https://doi:10.1111/j.1751-908X.2003.tb00710.x

Torresi I, Xavier RP, Bortholoto DFA, Monteiro LVS (2012) Hydrothermal alteration, fluid inclusions and stable isotope systematics of the Alvo 118 iron oxide-copper-gold deposit, Carajás Mineral Province (Brazil): Implications for ore genesis. Miner Depos 47:299–323. https://doi:10.1007/s00126-011-0373-4

Vasquez ML, Rosa-Costa LT, Silva CMG et al (2008) Geologia e Recursos Minerais do Estado do Pará: Sistema de Informações Geográficas - SIG: texto explicativo dos mapas Geológico e Tectônico e de Recursos Minerais do Estado do Pará. Escala 1:1.000.000. CPRM, Belém

Volp KM (2005) The Estrela copper deposit, Carajás, Brazil: Geology and implications of a Proterozoic copper stockwork. Miner Depos Res Meet Glob Chall - Proc Eighth Bienn SGA Meet 1085–1088

Wirth KR, Gibbs AK, Olszewski Jr. WJ (1986) U-Pb ages of zircons from the Grão-Pará Group and Serra dos Carajás Granites, Pará, Brazil. Rev Bras Geociências 16:195–200

Xavier RP, Araújo CEG, Dreher AM et al (2005) Fluid evolution in the Paleoproterozoic Intrusion-Related Breves Cu-Au-(Mo-W-Bi-Sn) deposit, Carajás Mineral Province, Northern Brazil. In: Horbe AMC, Souza VS (eds) Contribuições à Geologia da Amazônia. SBG-Núcleo Norte, pp 129–137

Xavier RP, Monteiro LVS, Moreto CPN et al (2012) The iron oxide copper-gold systems of the Carajás mineral province. Econ Geol 16:433–454

Xavier RP, Moreto CPN, Melo GHC et al (2017) Geology and Metallogeny of Neoarchean and Paleoproterozoic Copper Systems of the Carajás Domain, Amazonian Craton, Brazil. In: 14th SGA Biennial Meeting. SGA, Quebéc, pp 899–902

Xavier RP, Rusk B, Emsbo P, Monteiro LVS (2009) Composition and source of salinity of ore-bearing fluids in Cu-Au systems of the Carajás Mineral Province, Brazil. In: 10th SGA Biennial Meeting. SGA, Townsville, pp 272–274

Xavier RP, Trumbull RB, Wiedenbeck M, Monteiro LVS (2013) Sources of mineralizing fluids in Cu-Au systems from the Carajás Mineral Province (Brazil): constraints from in-situ microanalysis of hydrogen and boron isotopes in tourmaline. In: 12th SGA Biennial Meeting. Uppsala, pp 1402–1405

Yang SY, Jiang SY, Palmer MR (2015) Chemical and boron isotopic compositions of tourmaline from the Nyalam leucogranites, South Tibetan Himalaya: Implication for their formation from B-rich melt to hydrothermal fluids. Chem Geol 419:102–113. https://doi:10.1016/j.chemgeo.2015.10.026

Yavuz F, Karakaya N, Yildirim DK et al (2014) A Windows program for calculation and classification of tourmaline-supergroup (IMA-2011). Comput Geosci 63:70–87. https://doi:10.1016/j.cageo.2013.10.012

Figure Captions

Fig. 1 a Location of the Carajás Province (black) within the Amazonian Craton (light gray), Brazil. **b** Compartmentation of the Carajás Province into the Rio Maria domain (south) and the Carajás Domain (north), this limited to the north by the Bacajá Domain. **c** Simplified geological map of the Carajás Domain. Note the spatial distribution of important cupriferous systems and the currently operating Cu mines, as well as the main regional structures. The red box shows the location of the Santa Lúcia deposit (modified from Costa et al. 2016). Abbreviations: IOCG = iron oxide copper-gold, VMS = volcanogenic massive sulfide

Fig. 2 Simplified geological map of the Santa Lúcia deposit area (modified from Lima 2002)

Fig. 3 Schematic stratigraphic sequence of the Santa Lúcia deposit based on two representative drill cores (FD014 and FD022). Abbreviations: Ms = muscovite, Qz = quartz, Tur = tourmaline

Fig. 4 Drill core samples showing the main aspects of the Santa Lúcia deposit lithotypes. **a** Weakly to **b** moderately mylonitized chlorite-altered subvolcanic rock. **c** Bipyramidal phenocrysts of bluish quartz within a relatively isotropic subvolcanic rock. Note its greenish-to-grayish color due to chlorite (I) alteration. **d** Pegmatite intrusive body with quartz, microcline, muscovite, and tourmaline, intersecting the subvolcanic rock parallel and **e** oblique to its foliation. **f** Undeformed pegmatite intrusion composed of quartz, microcline, muscovite, and tourmaline. **g** Coarse-grained muscovite and tourmaline crystals within pegmatite. **h** Boudinaged tourmaline crystals intergrown with quartz and microcline. Abbreviations: Chl = chlorite, Mc = microcline, Ms = muscovite, Qz = quartz, Tur = tourmaline

Fig. 5 Photomicrographs showing the main features of the Santa Lúcia deposit lithotypes. **a** Least deformed subvolcanic rock of rhyolitic composition, constituted of quartz, microcline and biotite (transmitted light/cross-polarized light [XPL]). **b** Bipyramidal quartz phenocryst surrounded by a fine-grained groundmass of quartz, microcline, and biotite, within the subvolcanic rock (transmitted light/XPL). **c**, **d** and **e** Pegmatite intrusive body with quartz, microcline, muscovite, tourmaline, and minor allanite (transmitted light/XPL). **f** Poikiloblastic tourmaline phenocryst riddled with quartz and microcline inclusions (transmitted light/XPL). **g** Tourmaline-rich domain associated with the pegmatite intrusion (transmitted light/plane-polarized light [PPL]). **h** Perthitic exsolution lamellae within microcline. Note the presence of muscovite (transmitted light/XPL). **i** Stretched muscovite crystal in association with quartz (transmitted light/XPL). Abbreviations: Aln = allanite, Bt = biotite, Mc = microcline, Ms = muscovite, Pl = plagioclase, Qz = quartz, Tur = tourmaline

Fig. 6 Main aspects of the chlorite and greisen alteration stages. **a** Photomicrograph of selective alteration of biotite by chlorite (I) in the subvolcanic rock (transmitted light/XPL). **b** Photomicrograph of chlorite (I) veinlet intersecting the subvolcanic rock (transmitted light/PPL). **c** Photomicrograph of epidote aggregates associated with the early chlorite alteration stage. Note the partial replacement of biotite by chlorite (I) (transmitted light/PPL). **d** Photomicrograph of potassic alteration with microcline, overprinted by muscovite and quartz from the greisenization stage. Note the presence of hematite mantling both microcline and muscovite (transmitted light/PPL). **e** Drill core sample of reddish hydrothermal microcline coated by hematite. **f** Photomicrograph of hydrothermal microcline partially altered by muscovite and quartz (transmitted light/XPL). **g** Photomicrograph of quartz-tourmaline-muscovite-rich assemblage associated with the greisen alteration (transmitted light/XPL). **h** Photomicrograph of greisenized domains with tourmaline, muscovite, quartz, and chlorite (II) formed parallel to the rock foliation (transmitted light/PPL). **i** Drill core sample of muscovite/tourmaline-rich alteration halo in the contact between the pegmatite and the subvolcanic rock. **j** Photomicrograph of muscovite and chlorite (II) in apparent equilibrium, showing straight grain boundaries (transmitted light/XPL). **k** Photomicrograph of chlorite (II) infillings through muscovite cleavage (transmitted light/PPL). **l** Drill core sample of milky quartz-tourmaline-muscovite vein

crosscutting the subvolcanic rock. Abbreviations: Bt = biotite, Chl = chlorite, Ep = epidote, Hem = hematite, Mc = microcline, Ms = muscovite, Qz = quartz, Tur = tourmaline

Fig. 7 Drill core samples displaying the main features of the brecciated ore zone of the Santa Lúcia deposit. **a** Mineralized breccia with massive chalcopyrite and subordinate pyrite, enclosing quartz crystals and fragments of the subvolcanic rock. **b** Breccia-style chalcopyrite mineralization hosted by the subvolcanic rock. **c** Tourmaline-muscovite-quartz enrichment in the main ore zone with chalcopyrite. **d** Clast-supported mineralized breccia with chalcopyrite and coarse-grained milky quartz crystals. **e** Massive chalcopyrite hosted in a breccia body with associated sphalerite and apatite. **f** Highly strained apatite and chalcopyrite in ore breccia. Abbreviations: Ap = apatite, Chl = chlorite, Ccp = chalcopyrite, LF = lithic fragment, Ms = muscovite, Py = pyrite, Qz = quartz, Sp = sphalerite, Tur = tourmaline

Fig. 8 Photomicrographs showing the mineralization styles and the main aspects of the ore zone of the Santa Lúcia deposit, as well as the late sericite vein formation. **a** Chalcopyrite veinlet crosscutting quartz-rich zone in the subvolcanic rock (reflected light/PPL). **b** Chalcopyrite disseminations in the subvolcanic rock (reflected light/PPL). **c** Chalcopyrite-sphalerite-pyrrhotite-apatite association in breccia ore type sample (reflected light/PPL). **d** Tabular muscovite crystals in association with quartz and chalcopyrite (transmitted light/XPL). **e** Acicular sphalerite inclusions in carbonate, both surrounded by chalcopyrite and in association with quartz (transmitted light/XPL). **f** Tourmaline-chalcopyrite-allanite association in ore sample (transmitted light/PPL). **g** Allanite, muscovite and biotite inclusions in chalcopyrite (transmitted light/XPL). **h** Colloform sphalerite crystal in association with chalcopyrite (reflected light/PPL). **i** Xenoblastic sphalerite with chalcopyrite disease (reflected light/PPL). **j** Octahedral pentlandite exsolution along pyrrhotite rim, in contact with chalcopyrite (reflected light/PPL). **k** Idioblastic inclusions of pyrite in sphalerite (reflected light/PPL). **l** Tabular molybdenite crystal as inclusion in chalcopyrite (reflected light/PPL). **m** and **n** Backscattered electron (BSE) images showing sphalerite, pyrite, tellurobismuthite and cassiterite inclusions in chalcopyrite. **o** Sericite veinlet crosscutting pegmatite sample. Note the partial alteration of microcline by sericite in the upper-left corner (transmitted light/XPL). **p** Partial alteration of tourmaline by sericite in the pegmatite. The cloudy aspect of microcline (brownish color) is also due to incipient sericite alteration (transmitted light/PPL). Abbreviations: Aln = allanite, Ap = apatite, Bt = biotite, Cb = carbonate, Chl = chlorite, Ccp = chalcopyrite, Cst = cassiterite, Mc = microcline, Mol = molybdenite, Ms = muscovite, Pn = pentlandite, Po = pyrrhotite, Py = pyrite, Qz = quartz, Ser = sericite, Sp = sphalerite, Tb = tellurobismuthite, Tur = tourmaline

Figure 9 Main aspects of the post-ore hematite vein formation and fracture infilling. **a** Drill core sample of potassically altered zone with microcline, overprinted by hematite veinlets. **b** Photomicrograph of micro-faulted hydrothermal microcline partially altered to quartz and muscovite, and later crosscut by microcrystalline hematite veinlets

(transmitted light/XPL). **c** Drill core sample and **d** Photomicrograph of breccia zone showing angular fragments of the subvolcanic rock surrounded by a fine-grained hematite groundmass. Note the presence of hydrothermal microcline and sericite within the rock fragments (transmitted light/PPL). Abbreviations: Hem = hematite, Mc = microcline, Ms = muscovite, Qz = quartz, Ser = sericite

Fig. 10 Mineral paragenetic sequence of the Santa Lúcia hydrothermal system

Fig. 11 Rare earth element (REE) distribution patterns for the mineralized breccias of the Santa Lúcia deposit, evidencing a clear LREE enrichment. Chondrite values are from McDonough and Sun (1995)

Fig. 12 Photomicrographs of the selected tourmaline grains for boron isotope determinations. All photographs except **f** are under transmitted light/PPL. The yellow circles indicate spots of LA-MA-ICP-MS analyses and their corresponding $\delta^{11}B$ values. **a**, **b**, **c**, **d** and **e** Pegmatite tourmaline samples associated with quartz. Note sericite occurring as fracture infillings. **f** Ore-related tourmaline in association with chalcopyrite and sphalerite (reflected light/PPL). Abbreviations: Ccp = chalcopyrite, Qz = quartz, Ser = sericite, Sp = sphalerite, Tur = tourmaline

Fig. 13 Plots of chemical compositions of tourmaline from the Santa Lúcia deposit expressed in terms of atomic ratios and atoms per formula unit (a.p.f.u.). **a** X-site vacancy-Ca-Na ternary diagram after Henry et al. (2011). **b** Al-Fe-Mg ternary diagram modified after Henry and Guidotti (1985). Numbers identify the following fields: (1) Li-rich granitoid pegmatites and aplites; (2) Lithium-poor granitoids and their associated pegmatites and aplites; (3) Ferric iron-rich quartz-tourmaline rocks (hydrothermally altered granites); (4) Metapelites and metapsammites coexisting with an Al-saturating phase; (5) Metapelites and metapsammites not coexisting with an Al-saturating phase; (6) Ferric iron-rich quartz-tourmaline rocks, calc-silicate rocks and metapelites; (7) Low-Ca metaultramafics and Cr, V-rich metasediments; (8) Metacarbonates and meta-pyroxenites. **c** Fe/(Fe+Mg) versus Ca/(Ca+Na). **d** Mg versus Fe_{tot}

Fig. 14 Photomicrographs showing the textural relationships between monazite and other ore-related mineral phases from the mineralized breccia zone of the Santa Lúcia deposit. **a** Prismatic-shaped monazite grains surrounded by chalcopyrite (transmitted light/XPL). **b** Oval-shaped monazite grains within apatite (transmitted light/XPL). **c** Monazite aggregates within apatite (transmitted light/XPL). **d** Prismatic-shaped monazite grain displaying equilibrium textures with chalcopyrite and pyrrhotite (reflected light/PPL). **e**, **f**, **g** and **h** Representative BSE images of analysed monazite grains. Locations of SHRIMP analyses are shown as yellow circles. All data are reported as $^{207}Pb/^{206}Pb$ ages (up to 10% discordant). Abbreviations: Ap = apatite, Ccp = chalcopyrite, Mnz = monazite, Po = pyrrhotite

Fig. 15 $^{206}Pb/^{238}U$ vs. $^{207}Pb/^{235}U$ diagram for the monazite from the ore zone of the Santa Lúcia deposit. The weighted average $^{207}Pb/^{206}Pb$ age (2688 ± 27 Ma, MSWD = 0.14) of the main concordant cluster (light blue ellipses) is shown

in the inset. The red ellipses represent younger, but still concordant ages (2071 ± 49 Ma and 2491 ± 44 Ma), also recorded by the hydrothermal monazite grains

Fig. 16 Histogram of boron isotope compositions of tourmaline from the Santa Lúcia deposit. Data for the Breves deposit and IOCG systems of the Carajás Province (dark red lines) are from Xavier et al. (2013) and Xavier et al. (2008), respectively. Ranges of $\delta^{11}B$ values for global reservoirs in nature (dark green lines) are also shown for reference (Barth 1993; Marschall and Jiang 2011).

Table

Table 1. Boron isotope data of tourmaline from the Santa Lúcia deposit

Sample	$^{11}B/^{10}B$	$\delta^{11}B$ (‰)	Internal Precision (RSD, ‰)
Pegmatite			
FD14/113.30 - 1	4.5840	-2.6	0.3
FD14/113.30 - 2	4.5801	-3.5	0.4
FD14/113.30 - 3	4.5841	-2.6	0.4
FD14/113.30 - 4	4.5795	-3.6	0.4
FD14/113.30 - 5	4.5794	-3.6	0.4
FD14/113.30 - 6	4.5790	-3.7	0.3
FD14/113.30 - 7	4.5863	-2.1	0.4
FD14/113.30 - 8	4.5870	-1.9	0.4
FD14/113.30 - 9	4.5879	-1.7	0.4
FD14/113.30 - 10	4.5855	-2.3	0.4
Ore			
FD14/58.60 - 1	4.5885	-1.4	0.4
FD14/58.60 - 2	4.5871	-1.8	0.4
FD14/58.60 - 3	4.5866	-1.9	0.4
FD14/58.60 - 4	4.5900	-1.1	0.4
FD14/58.60 - 5	4.5924	-0.6	0.4
FD14/58.60 - 6	4.5871	-1.7	0.4
FD14/58.60 - 7	4.5861	-2.0	0.4
FD14/58.60 - 8	4.5863	-1.9	0.4

Table 2. SHRIMP II U-Pb monazite data from the main ore zone of the Santa Lúcia deposit (sample FD22/80.10)

Spot	U (ppm)	Th (ppm)	$^{232}Th/^{238}U$	% $^{206}Pb_c$	$^{204}Pb/^{206}Pb$	1σ	$^{207}Pb^*/^{206}Pb^*$	1σ	$^{207}Pb^*/^{235}U$	1σ	$^{206}Pb^*/^{238}U$	1σ	Rho	Ages (Ma)		% Discordance
														$^{206}Pb/^{238}U$	$^{207}Pb/^{238}Pb$	
Concordant data (up to 10% discordant)																
N16-12.5-1	307	6.4	0.022	0.04	0.000031	45	0.186	1.8	12.1	2.8	0.472	2.1	0.76	2491 ± 44	2704 ± 30	9
N16-12.8-1	181	7.5	0.043	0.05	0.000034	58	0.164	2.4	9.7	4.1	0.429	3.4	0.82	2303 ± 66	2497 ± 40	9
N16-12.12-1	170	6.1	0.037	0.02	0.000012	101	0.184	2	12.1	2.4	0.475	1.4	0.59	2507 ± 30	2692 ± 32	8
N16-12.13-1	148	5.5	0.039	-	-0.00000031	100	0.184	1.7	12.3	3.7	0.484	3.2	0.88	2543 ± 68	2690 ± 29	7
N16-12.14-1	264	9.9	0.039	-	-0.00000037	7.7E+09	0.128	2.8	6	3.7	0.342	2.5	0.68	1895 ± 42	2071 ± 49	10
N16-12.15-1	220	6.1	0.029	-	-0.0000069	100	0.183	2	12.6	2.4	0.498	1.3	0.54	2604 ± 27	2682 ± 33	4
N16-12.16-1	237	11	0.048	0.06	0.000043	41	0.182	1.7	11.9	3.6	0.475	3.1	0.88	2504 ± 65	2674 ± 29	8
Discordant and/or high common Pb data																
N16-12.1-1	112	5.8	0.053	0.13	0.000096	41	0.168	1.8	9.1	3	0.39	2.4	0.79	2125 ± 43	2541 ± 31	19
N16-12.2-1	365	1.7	0.005	0.05	0.000038	41	0.185	2	11.1	2.4	0.437	1.5	0.6	2339 ± 29	2694 ± 32	16
N16-12.3-1	390	18.7	0.049	0.01	0.0000058	103	0.146	1.7	7.7	2.4	0.381	1.7	0.71	2081 ± 30	2298 ± 29	11
N16-12.4-1	160	6.5	0.042	0.1	0.000073	45	0.188	1.8	12	2.8	0.463	2.2	0.77	2452 ± 44	2723 ± 29	12
N16-12.6-1	84	0.5	0.007	-	-0.000000087	1414214	0.191	3.7	11.1	6.1	0.423	4.8	0.79	2275 ± 93	2750 ± 61	20
N16-12.7-1	8	28.7	3.559	2	0.0012	51	0.094	11.9	4	12.7	0.305	4.5	0.35	1714 ± 68	1514 ± 225	-15
N16-12.9-1	188	7.7	0.042	-	-0.00000035	1414214	0.185	1.8	11.2	2.3	0.438	1.4	0.62	2343 ± 28	2698 ± 29	16
N16-12.10-1	31	12.1	0.401	-	-0.0000039	816497	0.117	5.6	5	6.1	0.308	2.3	0.38	1732 ± 35	1910 ± 100	11
N16-12.11-1	310	21.7	0.072	-	-0.0000076	100	0.182	1.7	11.5	2.4	0.458	1.6	0.68	2433 ± 33	2670 ± 29	11

% $^{206}Pb_c$ represents the proportion of ^{206}Pb from common Pb. Pb* indicates radiogenic Pb, corrected for common Pb.

Figure

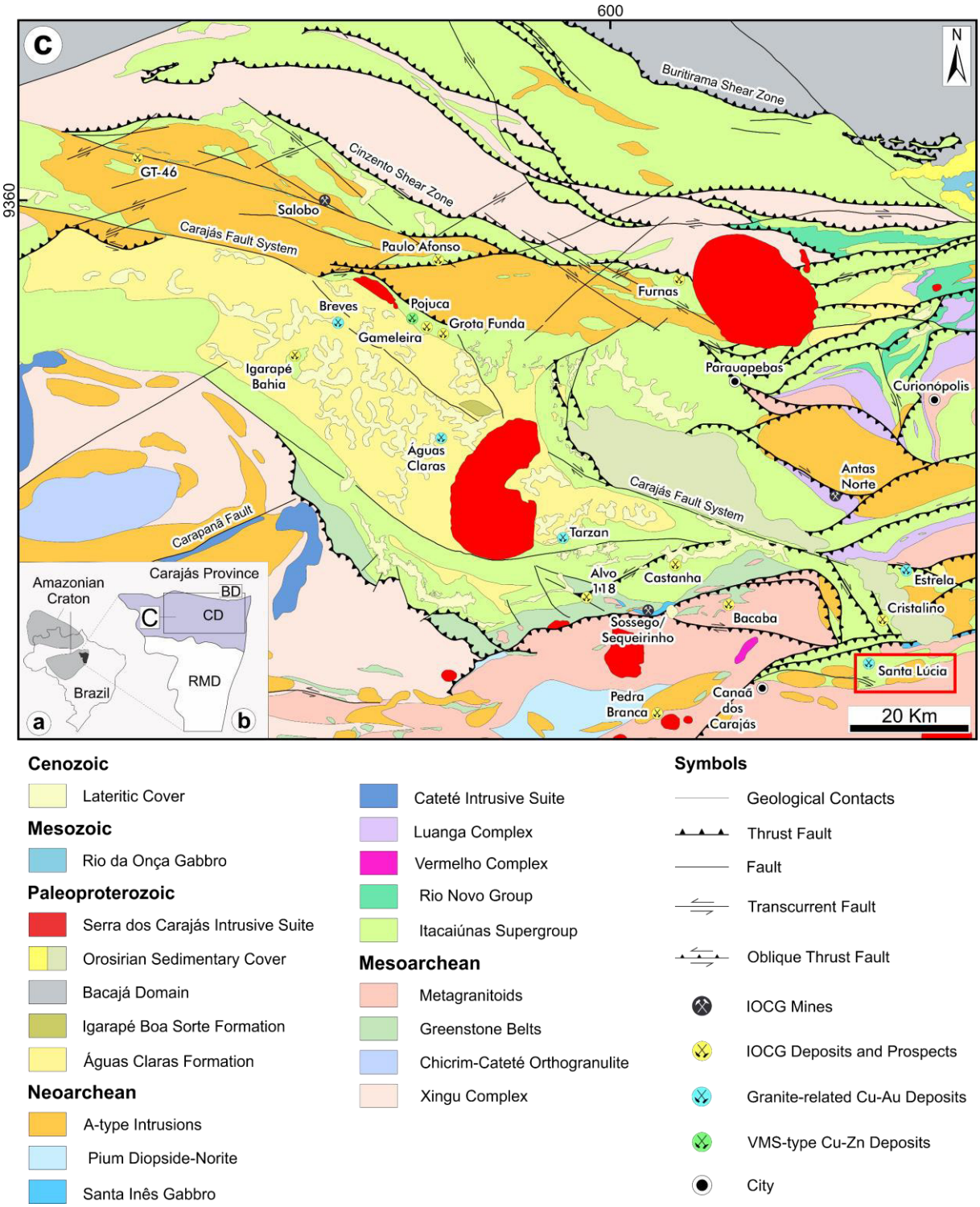
600
9360
c
N
Buritirama Shear Zone
Cinzento Shear Zone
GT-46
Salobo
Carajás Fault System
Paulo Afonso
Pojuca
Breves
Grota Funda
Gameleira
Furnas
Igarapé Bahia
Parauapebas
Curionópolis
Águas Claras
Antas Norte
Carajás Fault System
Carapanã Fault
Tarzan
Alvo 118
Castanha
Estrela
Cristalino
Sossego/ Sequeirinho
Bacaba
Santa Lúcia
Pedra Branca
Canaã dos Carajás
20 Km
Amazonian Craton
Carajás Province
BD
C
CD
RMD
Brazil
a
b
Cenozoic
Lateritic Cover
Mesozoic
Rio da Onça Gabbro
Paleoproterozoic
Serra dos Carajás Intrusive Suite
Orosirian Sedimentary Cover
Bacajá Domain
Igarapé Boa Sorte Formation
Águas Claras Formation
Neoarchean
A-type Intrusions
Pium Diopside-Norite
Santa Inês Gabbro
Cateté Intrusive Suite
Luanga Complex
Vermelho Complex
Rio Novo Group
Itacaiúnas Supergroup
Mesoarchean
Metagranitoids
Greenstone Belts
Chicrim-Cateté Orthogranulite
Xingu Complex
Symbols
Geological Contacts
Thrust Fault
Fault
Transcurrent Fault
Oblique Thrust Fault
IOCG Mines
IOCG Deposits and Prospects
Granite-related Cu-Au Deposits
VMS-type Cu-Zn Deposits
City

Fig. 1

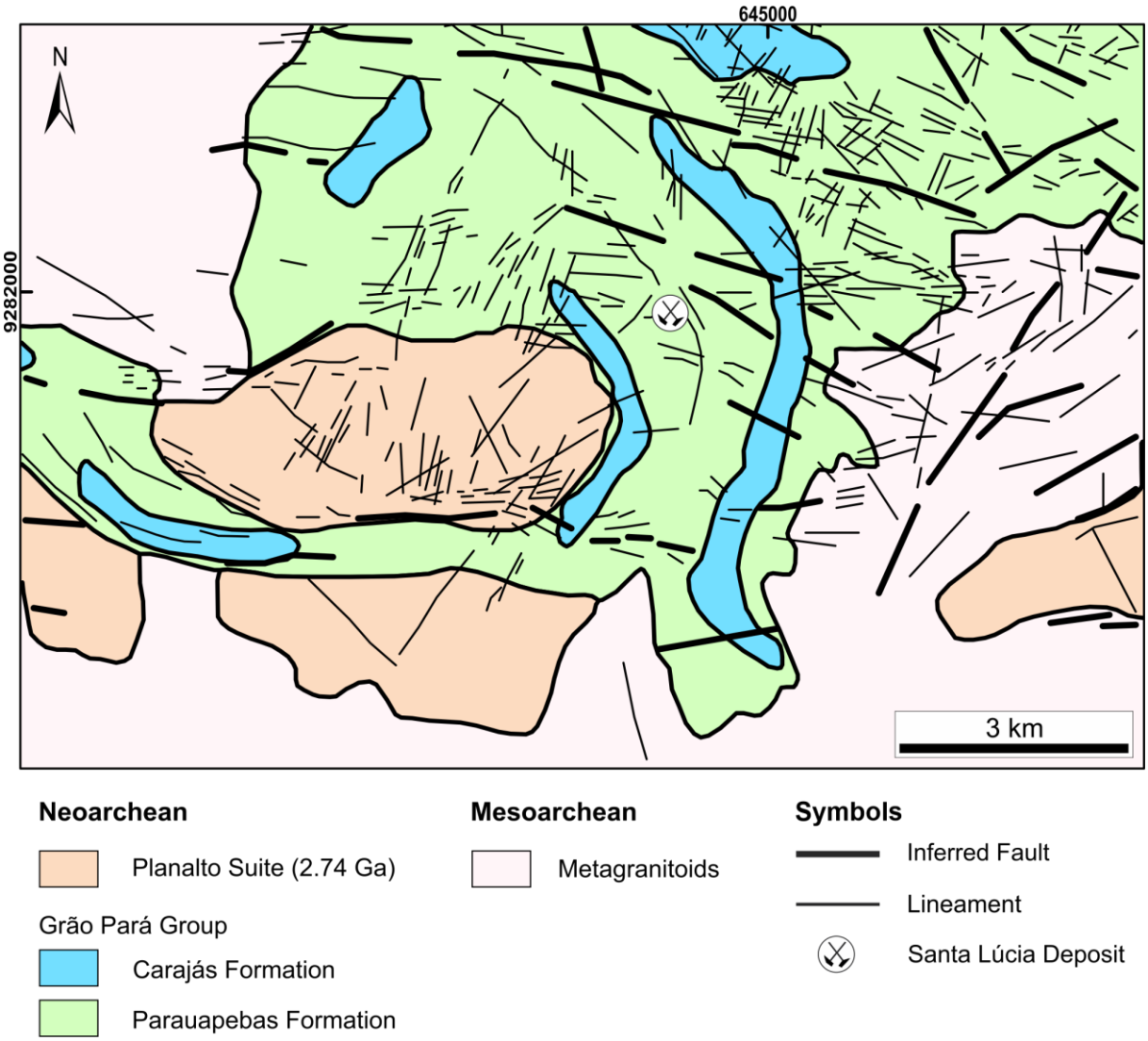
645000
9282000
N
3 km
Neoarchean
Planalto Suite (2.74 Ga)
Grão Pará Group
Carajás Formation
Parauapebas Formation
Mesoarchean
Metagranitoids
Symbols
Inferred Fault
Lineament
Santa Lúcia Deposit

Fig. 2

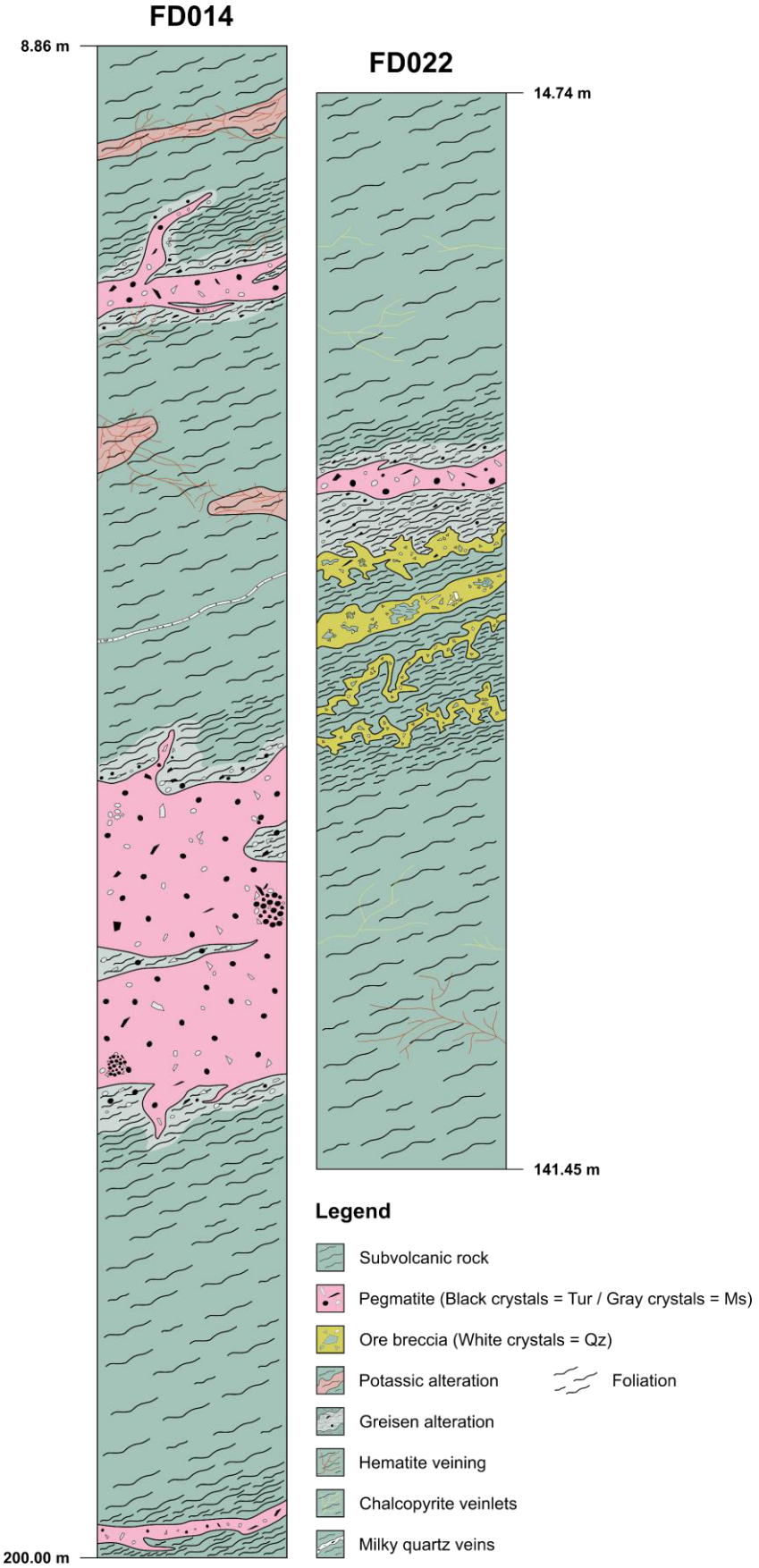
FD014
8.86 m
200.00 m
FD022
14.74 m
141.45 m
Legend
Subvolcanic rock
Pegmatite (Black crystals = Tur / Gray crystals = Ms)
Ore breccia (White crystals = Qz)
Potassic alteration
Foliation
Greisen alteration
Hematite veining
Chalcopyrite veinlets
Milky quartz veins

Fig. 3

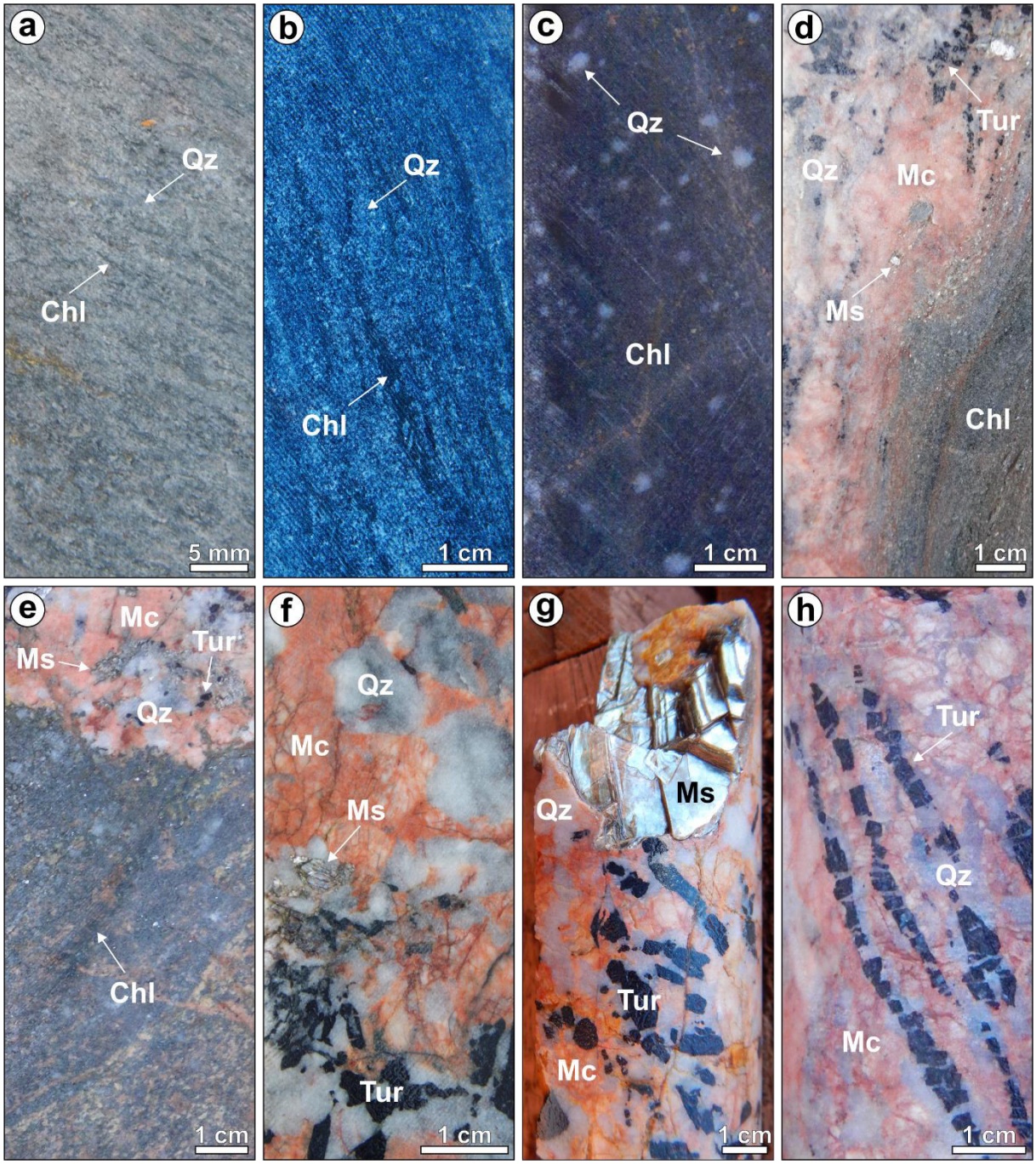
a
Qz
Chl
5 mm
b
Qz
Chl
1 cm
c
Qz
Chl
1 cm
d
Tur
Qz
Mc
Ms
Chl
1 cm
e
Mc
Tur
Ms
Qz
Chl
1 cm
f
Qz
Mc
Ms
Tur
1 cm
g
Ms
Qz
Tur
Mc
1 cm
h
Tur
Qz
Mc
1 cm

Fig. 4

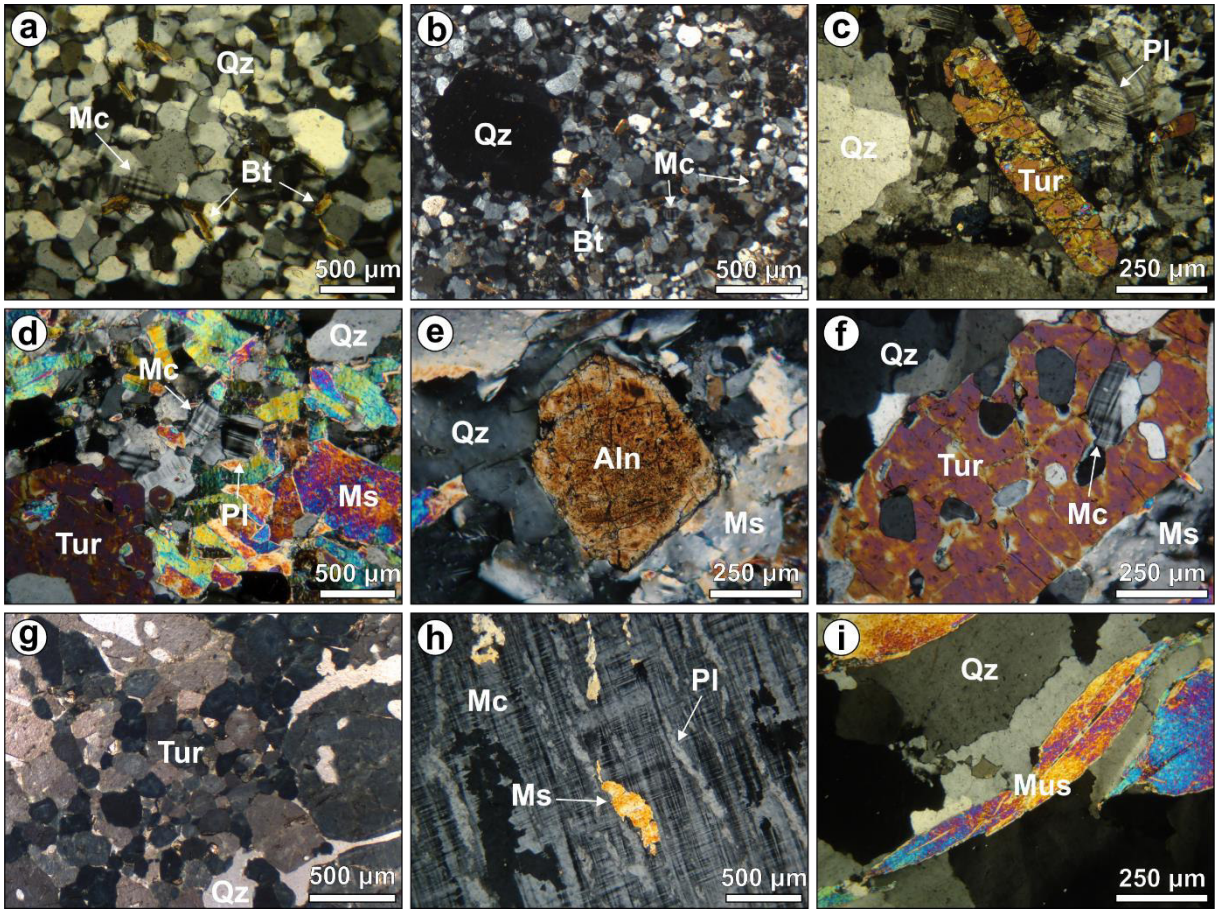
a
Qz
Mc
Bt
500 µm
b
Qz
Mc
Bt
500 µm
c
Pl
Qz
Tur
250 µm
d
Mc
Qz
Pl
Ms
Tur
500 µm
e
Qz
Aln
Ms
250 µm
f
Qz
Tur
Mc
Ms
250 µm
g
Tur
Qz
500 µm
h
Mc
Pl
Ms
500 µm
i
Qz
Mus
250 µm

Fig. 5

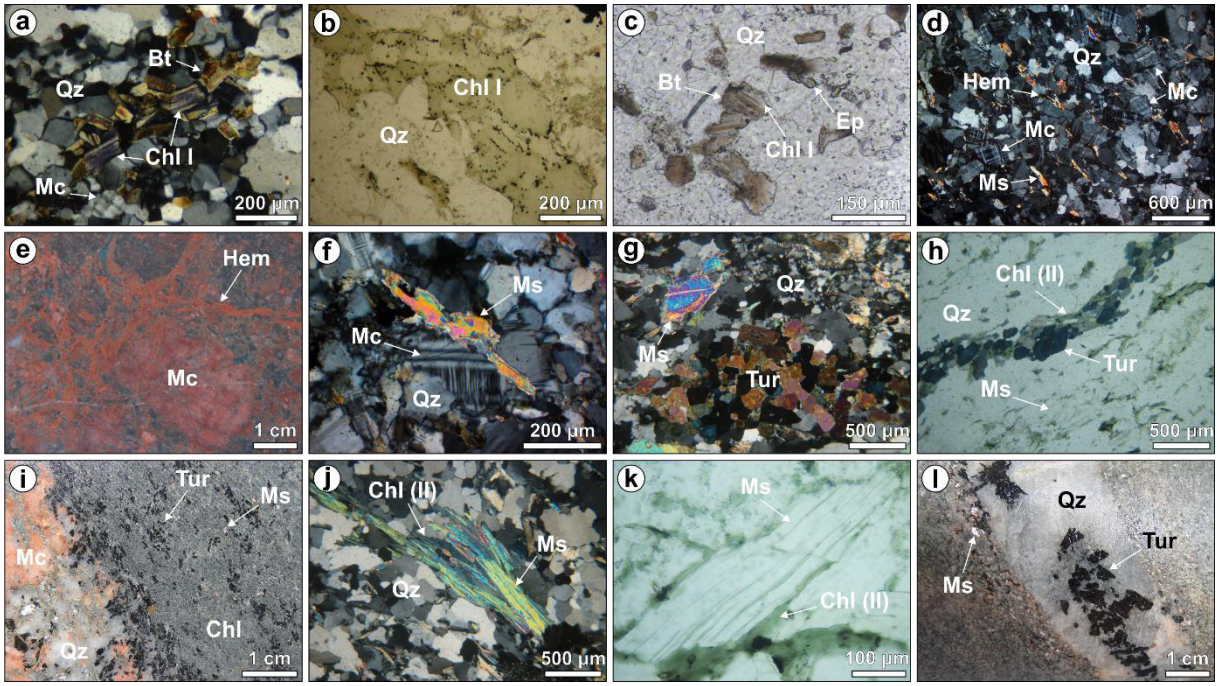
a
Bt
Qz
Chl I
Mc
200 µm
b
Chl I
Qz
200 µm
c
Qz
Bt
Ep
Chl I
150 µm
d
Qz
Hem
Mc
Mc
Ms
600 µm
e
Hem
Mc
1 cm
f
Ms
Mc
Qz
200 µm
g
Qz
Ms
Tur
500 µm
h
Chl (II)
Qz
Tur
Ms
500 µm
i
Tur
Ms
Mc
Chl
Qz
1 cm
j
Chl (II)
Ms
Qz
500 µm
k
Ms
Chl (II)
100 µm
l
Qz
Tur
Ms
1 cm

Fig. 6

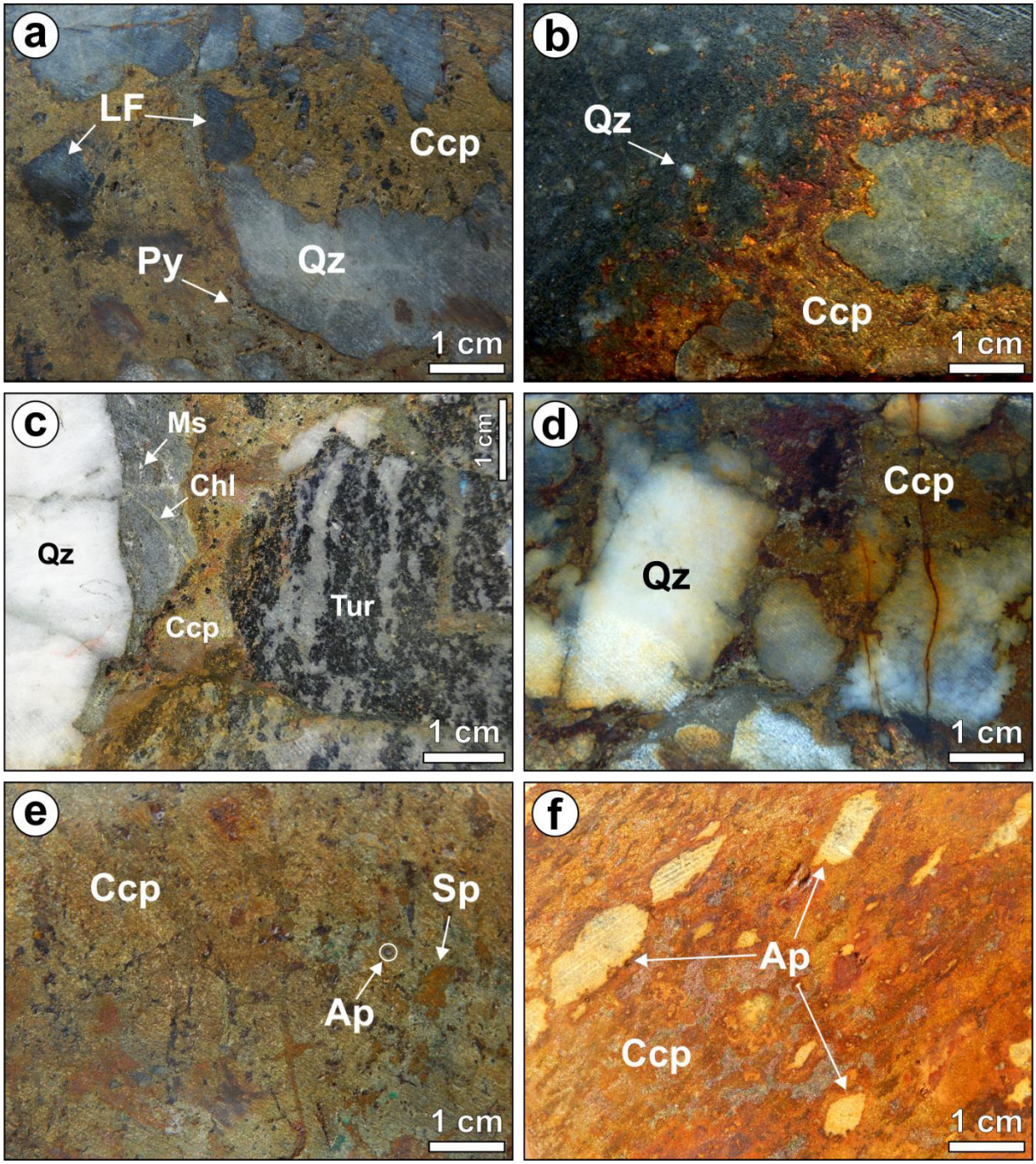
a
LF
Ccp
Py
Qz
1 cm
b
Qz
Ccp
1 cm
c
Ms
Chl
Qz
Ccp
Tur
1 cm
1 cm
d
Ccp
Qz
1 cm
e
Ccp
Sp
Ap
1 cm
f
Ap
Ccp
1 cm

Fig. 7

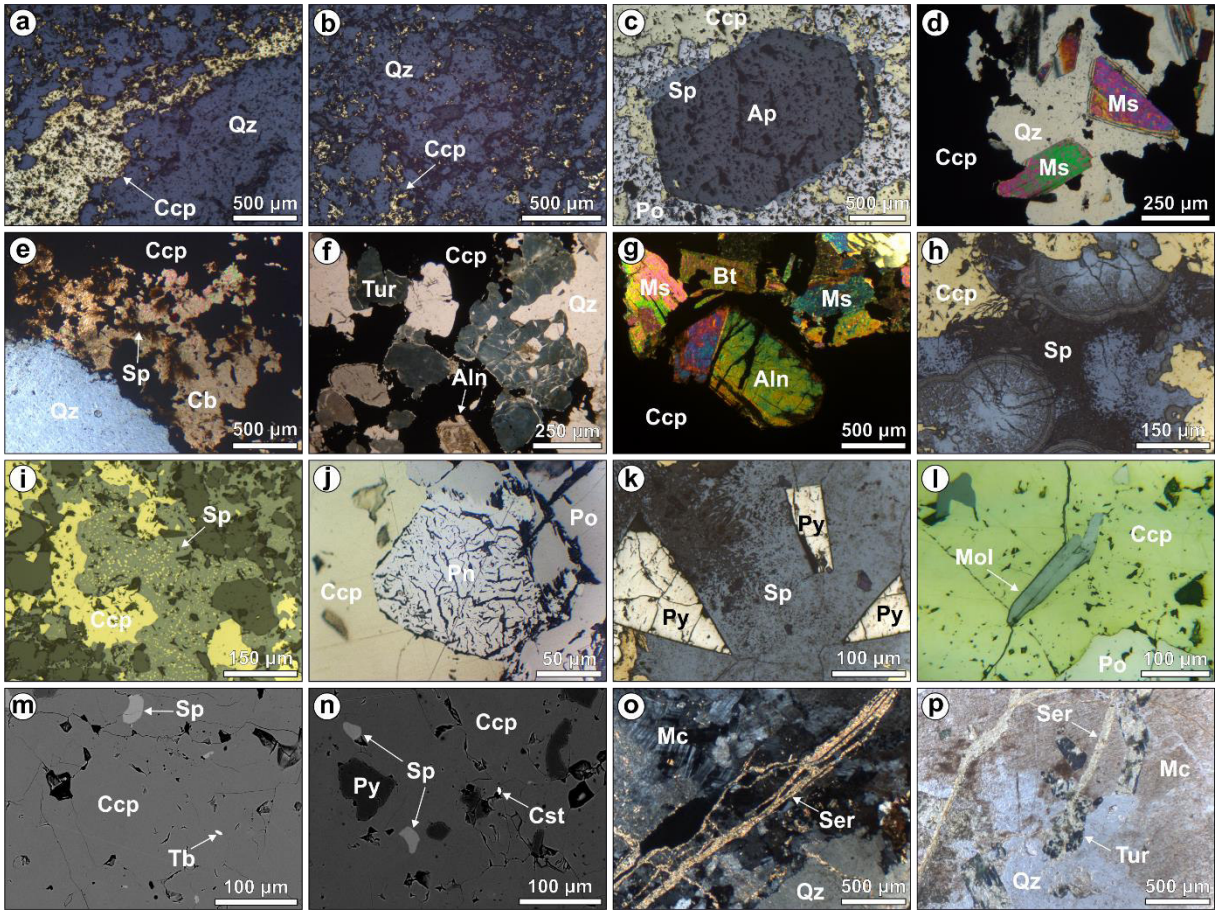
a
Qz
Ccp
500 µm
b
Qz
Ccp
500 µm
c
Ccp
Sp
Ap
Po
500 µm
d
Ms
Qz
Ccp
Ms
250 µm
e
Ccp
Sp
Cb
Qz
500 µm
f
Ccp
Tur
Qz
Aln
250 µm
g
Ms
Bt
Ms
Aln
Ccp
500 µm
h
Ccp
Sp
150 µm
i
Sp
Ccp
150 µm
j
Po
Ccp
Pn
50 µm
k
Py
Sp
Py
Py
100 µm
l
Ccp
Mol
Po
100 µm
m
Sp
Ccp
Tb
100 µm
n
Ccp
Py
Sp
Cst
100 µm
o
Mc
Ser
Qz
500 µm
p
Ser
Mc
Tur
Qz
500 µm

Fig. 8

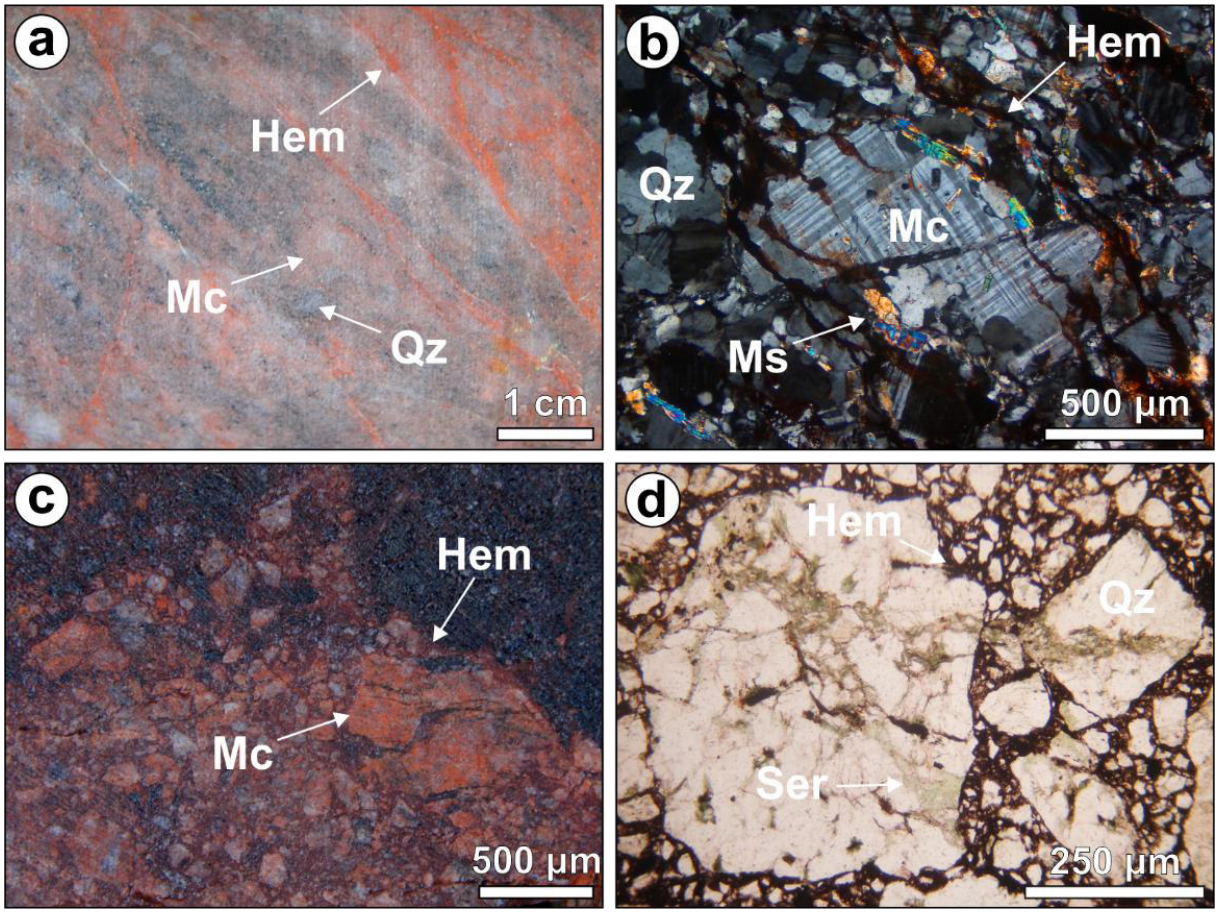
a
Hem
Mc
Qz
1 cm
b
Hem
Qz
Mc
Ms
500 µm
c
Hem
Mc
500 µm
d
Hem
Qz
Ser
250 µm

Figure 9

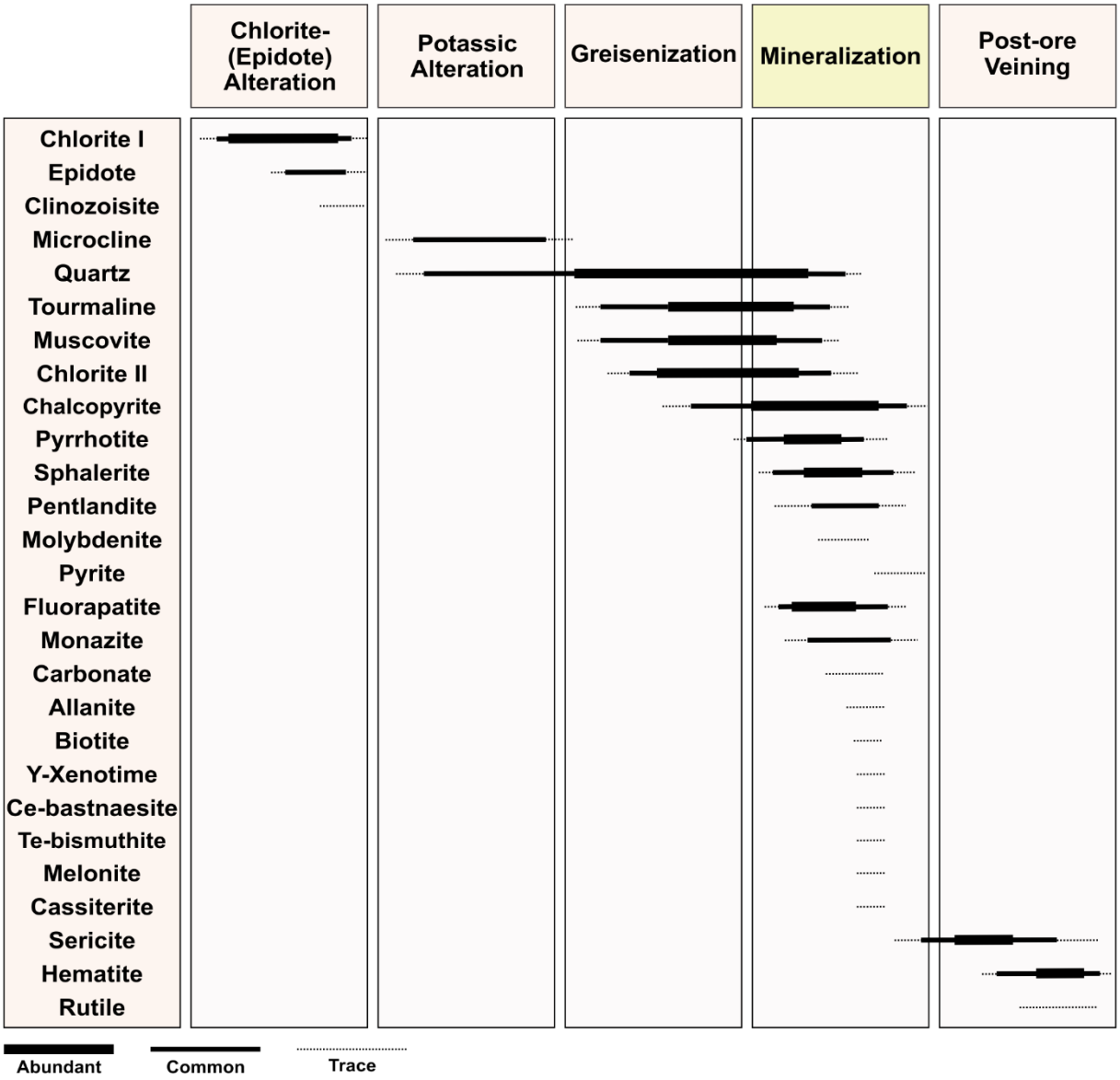
Chlorite-(Epidote) Alteration
Potassic Alteration
Greisenization
Mineralization
Post-ore Veining
Chlorite I
Epidote
Clinozoisite
Microcline
Quartz
Tourmaline
Muscovite
Chlorite II
Chalcopyrite
Pyrrhotite
Sphalerite
Pentlandite
Molybdenite
Pyrite
Fluorapatite
Monazite
Carbonate
Allanite
Biotite
Y-Xenotime
Ce-bastnaesite
Te-bismuthite
Melonite
Cassiterite
Sericite
Hematite
Rutile
Abundant
Common
Trace

Fig. 10

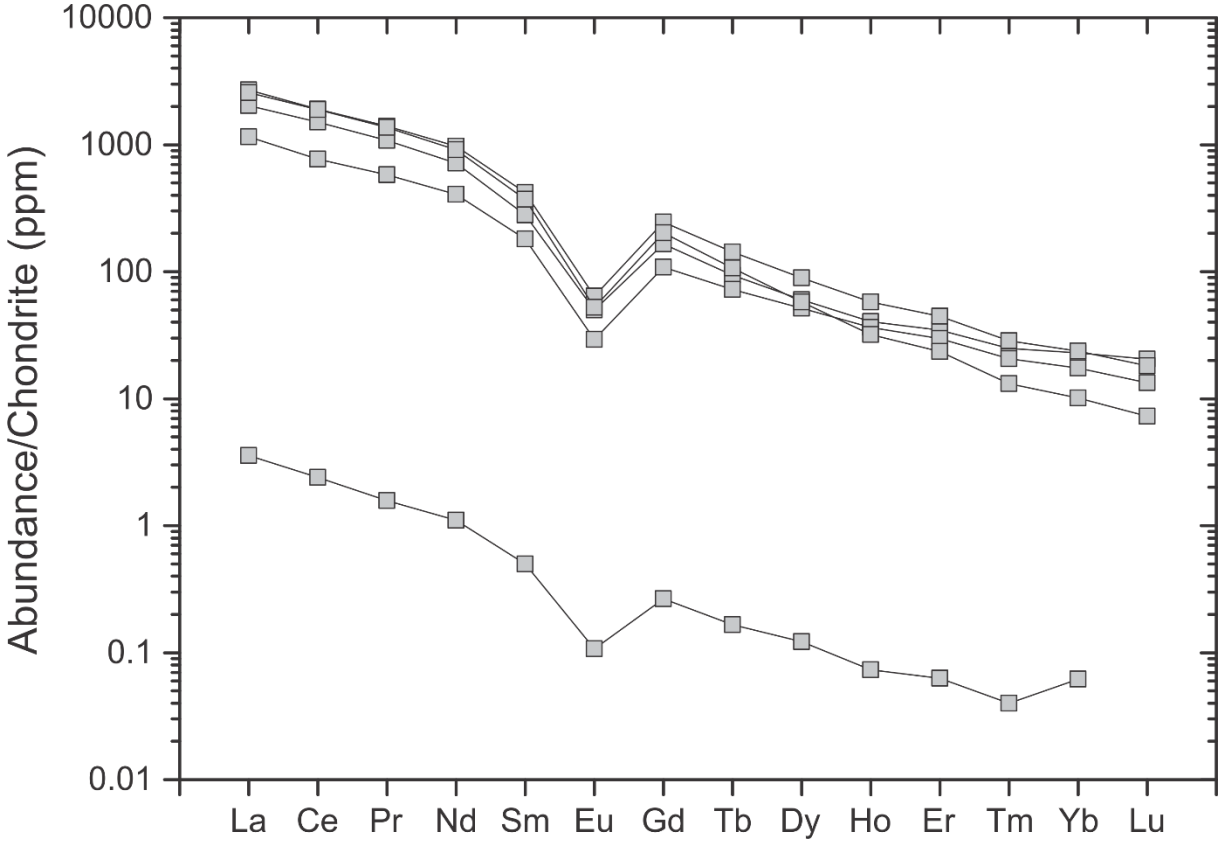
10000
1000
100
10
1
0.1
0.01
Abundance/Chondrite (ppm)
La
Ce
Pr
Nd
Sm
Eu
Gd
Tb
Dy
Ho
Er
Tm
Yb
Lu

Fig. 11

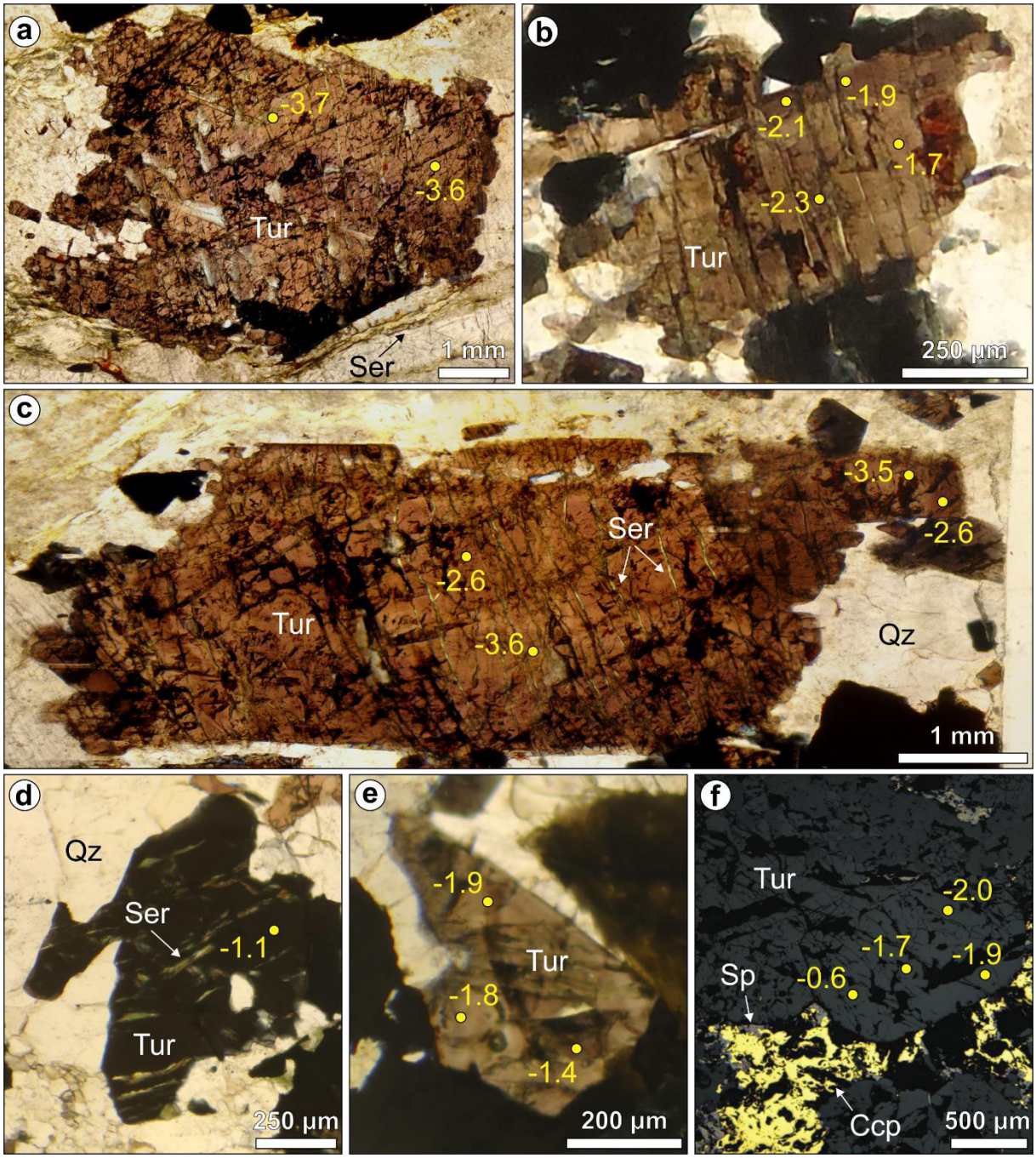
a
-3.7
-3.6
Tur
Ser
1 mm
b
-1.9
-2.1
-1.7
-2.3
Tur
250 µm
c
-3.5
-2.6
Ser
-2.6
Tur
-3.6
Qz
1 mm
d
Qz
Ser
-1.1
Tur
250 µm
e
-1.9
Tur
-1.8
-1.4
200 µm
f
Tur
-2.0
-1.7
-1.9
Sp
-0.6
Ccp
500 µm

Fig. 12

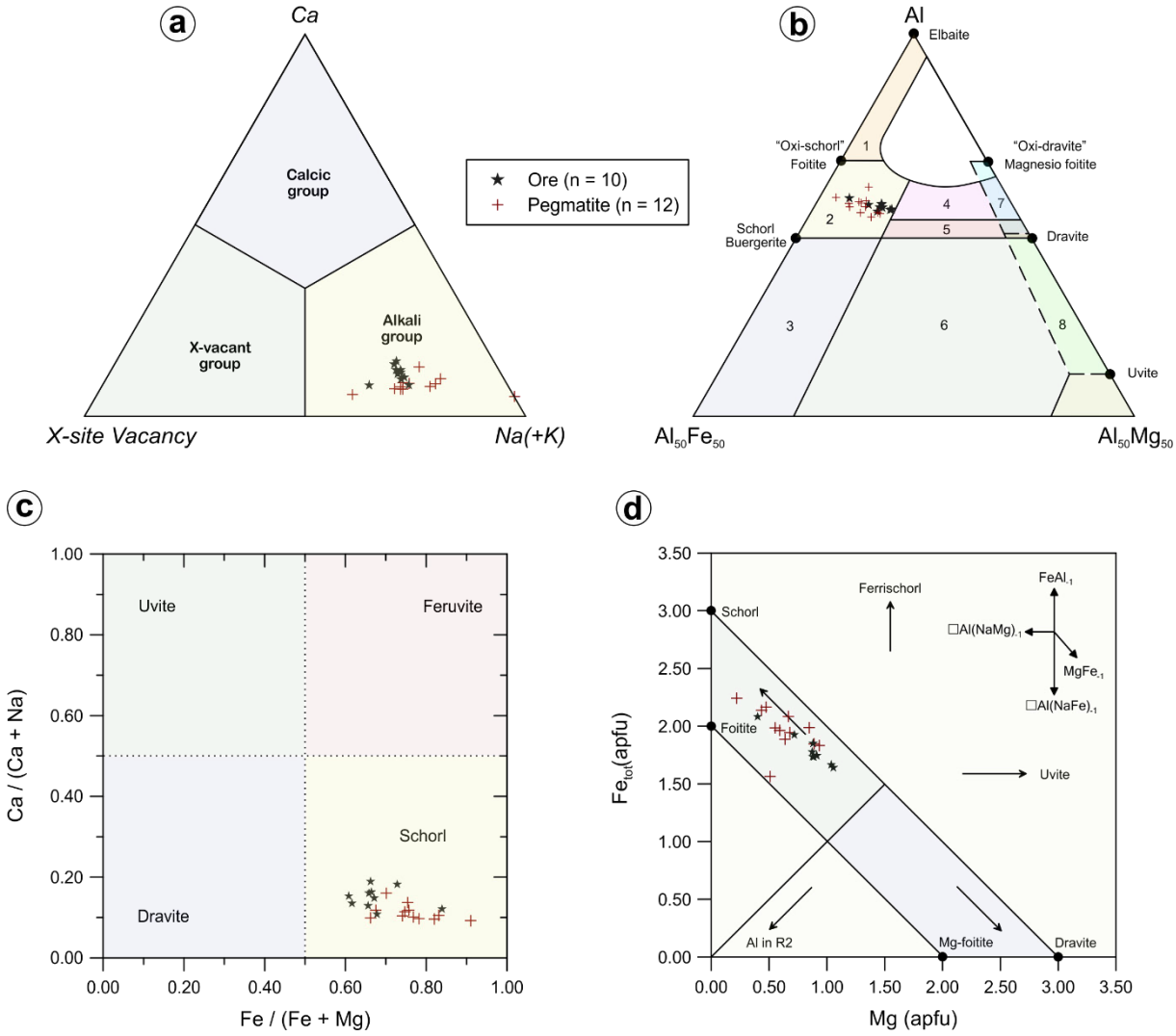
a
Ca
Calcic group
X-vacant group
Alkali group
X-site Vacancy
Na(+K)
Ore (n = 10)
Pegmatite (n = 12)
b
Al
Elbaite
"Oxi-schorl"
Foitite
"Oxi-dravite"
Magnesio foitite
Schorl
Buergerite
Dravite
Uvite
1
2
3
4
5
6
7
8
Al50Fe50
Al50Mg50
c
Uvite
Feruvite
Schorl
Dravite
Ca / (Ca + Na)
Fe / (Fe + Mg)
d
Schorl
Foitite
Ferrischorl
FeAl-1
□Al(NaMg)-1
MgFe-1
□Al(NaFe)-1
Uvite
Al in R2
Mg-foitite
Dravite
Fetot(apfu)
Mg (apfu)

Fig. 13

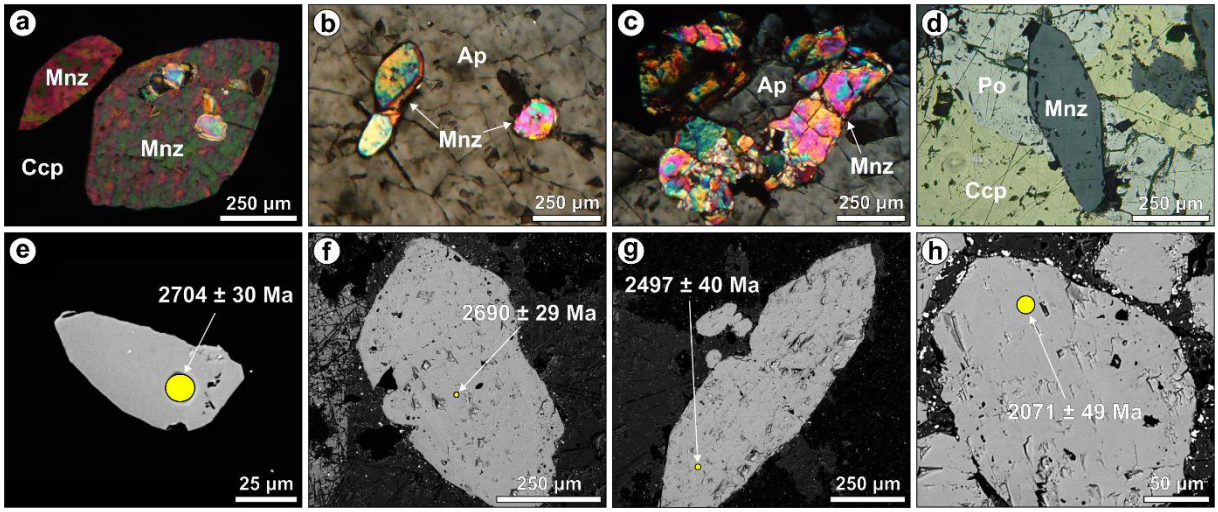
a
Mnz
Mnz
Ccp
250 µm
b
Ap
Mnz
250 µm
c
Ap
Mnz
250 µm
d
Po
Mnz
Ccp
250 µm
e
2704 ± 30 Ma
25 µm
f
2690 ± 29 Ma
250 µm
g
2497 ± 40 Ma
250 µm
h
2071 ± 49 Ma
50 µm

Fig. 14

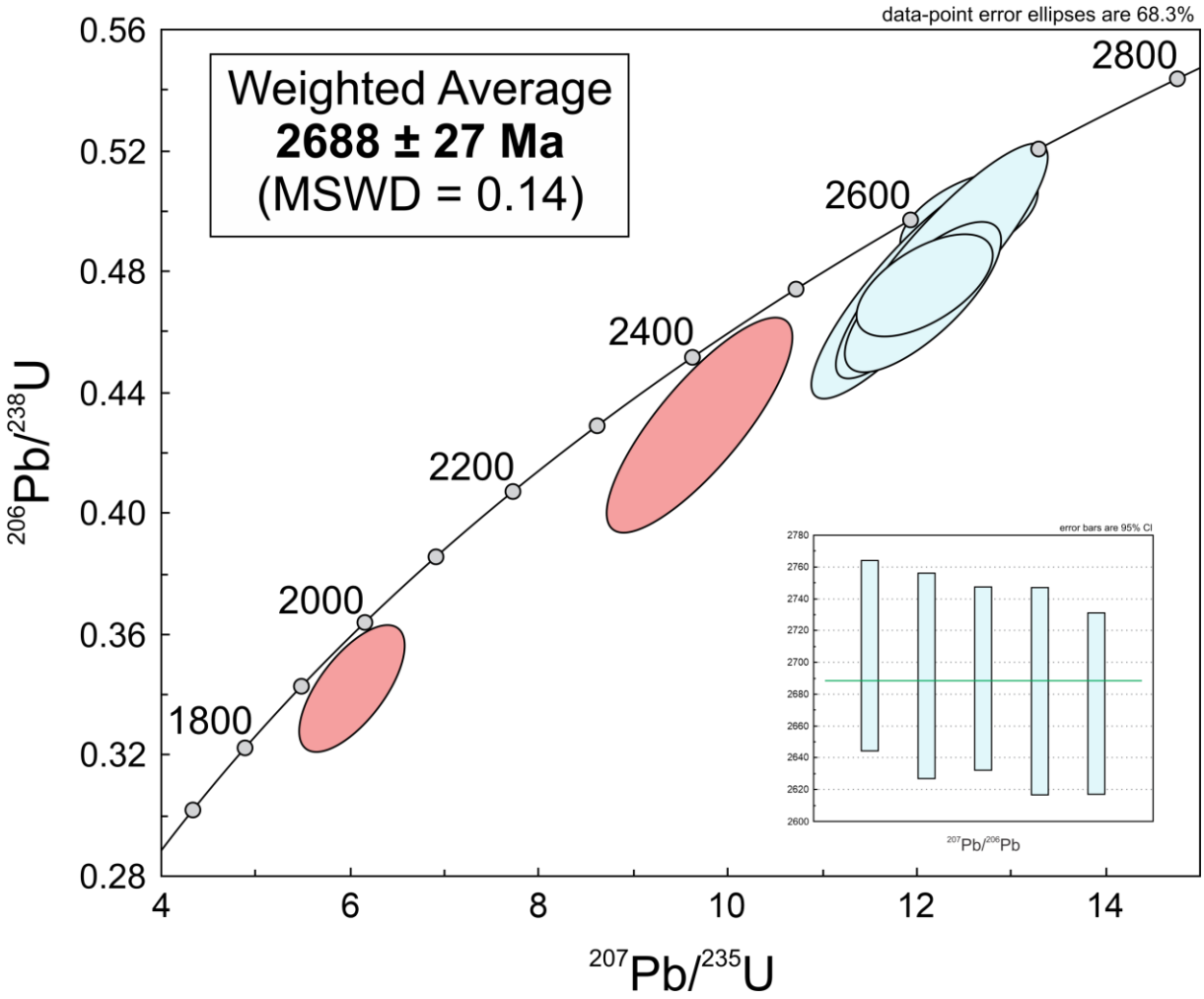
data-point error ellipses are 68.3%
Weighted Average
2688 ± 27 Ma
(MSWD = 0.14)
1800
2000
2200
2400
2600
2800
0.56
0.52
0.48
0.44
0.40
0.36
0.32
0.28
4
6
8
10
12
14
206Pb/238U
207Pb/235U
error bars are 95% CI
2780
2760
2740
2720
2700
2680
2660
2640
2620
2600
207Pb/206Pb

Fig. 15

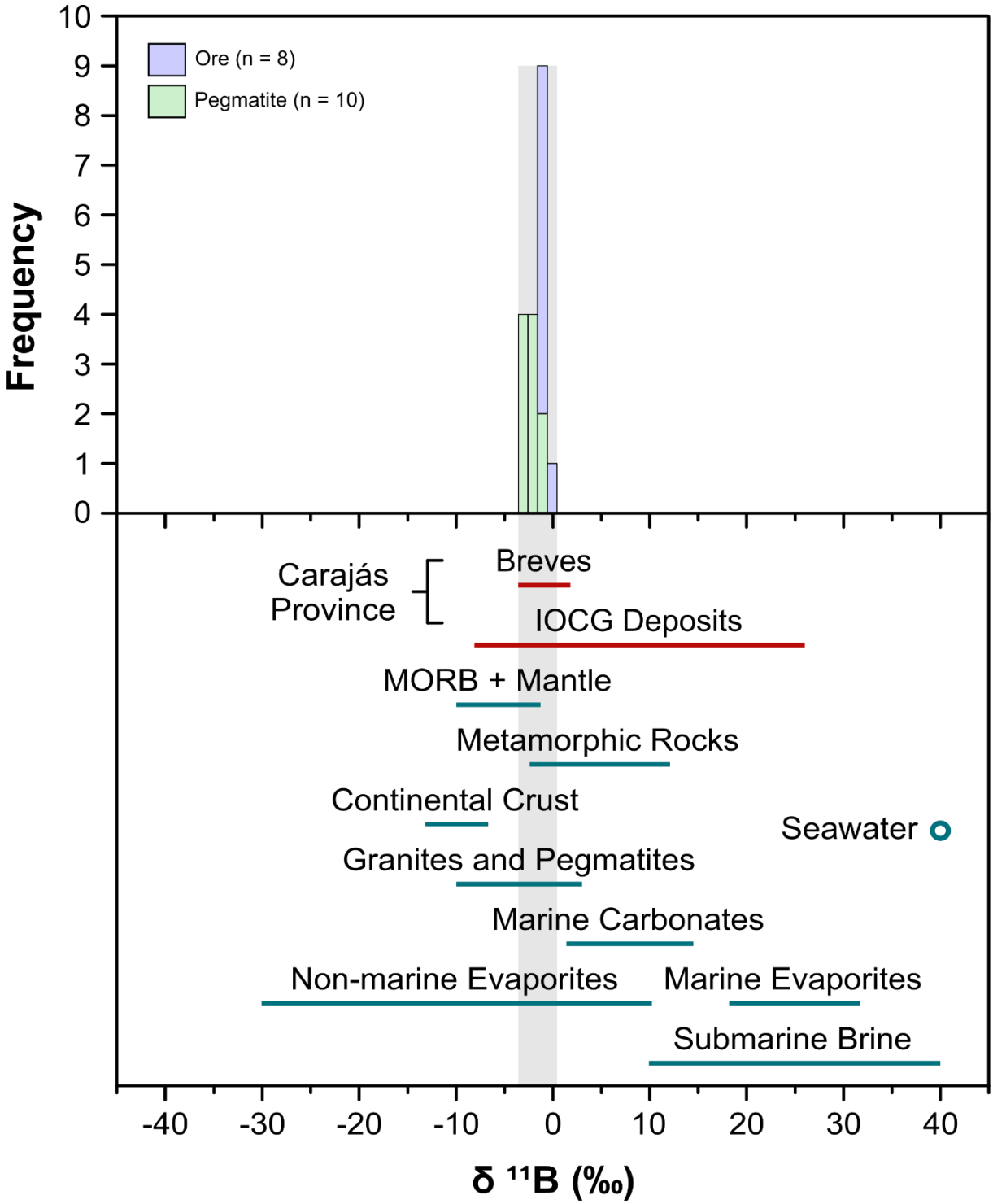
Ore (n = 8)
Pegmatite (n = 10)
Frequency
10
9
8
7
6
5
4
3
2
1
0
Carajás Province
Breves
IOCG Deposits
MORB + Mantle
Metamorphic Rocks
Continental Crust
Seawater
Granites and Pegmatites
Marine Carbonates
Non-marine Evaporites
Marine Evaporites
Submarine Brine
-40
-30
-20
-10
0
10
20
30
40
δ ¹¹B (‰)

Fig. 16